A Computational Study of Pressure Driven Flow in Waste Rock Piles

by

Jared Penney

A thesis
presented to the University of Waterloo
in fulfillment of the
thesis requirement for the degree of
Master of Mathematics
in
Applied Mathematics

Waterloo, Ontario, Canada, 2012

I hereby declare that I am the sole author of this thesis. This is a true copy of the thesis, including any required final revisions, as accepted by my examiners.

I understand that my thesis may be made electronically available to the public.

Abstract

This thesis is motivated by problems studied as part of the Diavik Waste Rock Pile Project. Located at the Diavik Diamond Mine in the Northwest Territories, with academic support from the University of Waterloo, the University of Alberta, and the University of British Columbia, this project focuses on constructing mine waste rock piles and studying their physical and chemical properties and the transport processes within them. One of the main reasons for this investigation is to determine the effect of environmental factors on acid mine drainage (AMD) due to sulfide oxidation and the potential environmental impact of AMD. This research is concerned with modeling pressure driven flow through waste rock piles. Unfortunately, because of the irregular shape of the piles, very little data for fluid flow about such an obstacle exists, and the numerical techniques available to work with this domain are limited. Since this restricts the study of the mathematics behind the flow, this thesis focuses on a cylindrical domain, since flow past a solid cylinder has been subjected to many years of study. The cylindrical domain also facilitates the implementation of a pseudo-spectral method.

This thesis examines a pressure driven flow through a cylinder of variable permeability subject to turbulent forcing. An equation for the steady flow of an incompressible fluid through a variable permeability porous medium is derived based on Darcy's law, and a pseudo-spectral model is designed to solve the problem. An unsteady time-dependent model for a slightly compressible fluid is then presented, and the unsteady flow through a constant permeability cylinder is examined. The steady results are compared with a finite element model on a trapezoidal domain, which provides a better depiction of a waste rock pile cross section.

Acknowledgements

First and foremost, I wish to extend my sincerest gratitude to my supervisor, Dr. Marek Stastna, for his guidance in my research and preparing this manuscript. I would also like to acknowledge the readers of this thesis and to thank them for their time. Retroactive thanks are extended to my former undergraduate research supervisors, Dr. Jahrul Alam, Dr. Danny Dyer, Dr. Chris Flinn, and Dr. Christina Bottaro. As always I am indebted to my family and loved ones for their unending support.

Dedication

To my family.

Table of Contents

List of Figures

Chapter 1

Introduction

1.1 Mine Site and Waste Rock Chemistry

The Diavik Diamond Mine is located nearly 300 km northeast of Yellowknife on a 20 km^2 island in Lac de Gras at 64.511389°N, 110.289722°W (Figure 1.1). Two large open pits are used to mine three separate bodies of diamond ore called kimberlite pipes, as presented in Figure 1.2. Currently a transition is being made at the site from open-pit mining to underground mining only [13]. The former involves the extraction of minerals from open pits or quarries in the ground, while the latter involves the digging of tunnels to access underground materials. The rock removed from the mines is called waste rock, and generally has a mineral content so low that recovery is economically unfeasible. This rock is stored on site in large stockpiles, sometimes referred to in the literature as heaps.

At the Diavik Mine, there are three piles of varying rock types being used for research purposes, indicated by TI, TIII, and TC in Figure 1.3. Each pile is about 15 m high with 20 m × 50 m upper surfaces, and angles of repose of approximately 37.5° for piles TI and TIII, and 18.4° for pile TC. The schematics for pile TIII can be found in Figure 1.4 [10].

The presence of sulfide minerals in waste rock can lead to acid mine drainage (AMD), a process through which acidic water run-off may be produced from the rock due to sulfide oxidation [10]. For the oxidation of pyrite, the sulfide mineral commonly found in waste rock, the overall chemical reaction is given as

$$2FeS_2 + 7O_2 + 2H_2O \rightarrow 2Fe^{2+} + 4SO_4^{2-} + 4H^+. \tag{1.1}$$

This reaction is highly exothermic, and for every mole of pyrite oxidized produces 1409 kJ

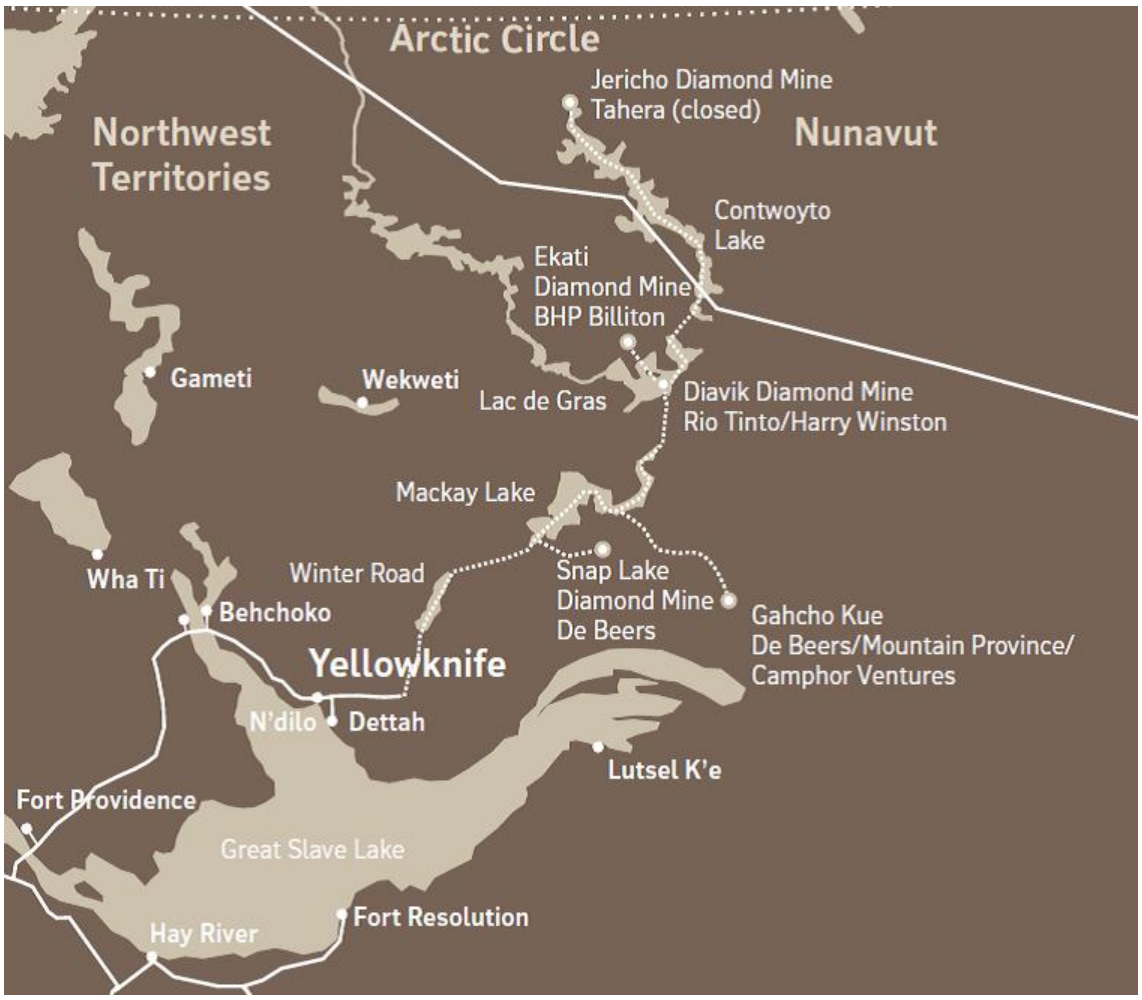

Figure 1.1: Map of the area surrounding the Diavik Diamond Mine [13].

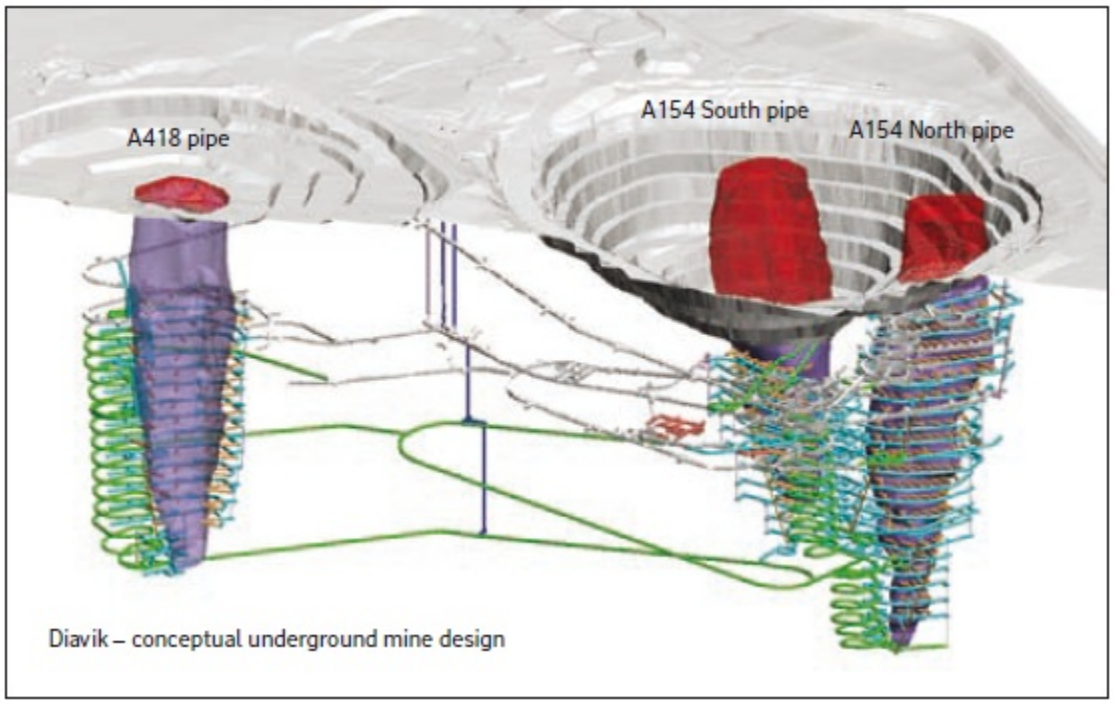

Figure 1.2: Conceptual diagram of the open pit mines, underground mines, and the kimberlite pipes. The red colouring indicates ore that has already been mined, while the purple colouring indicates the remaining ore [13].

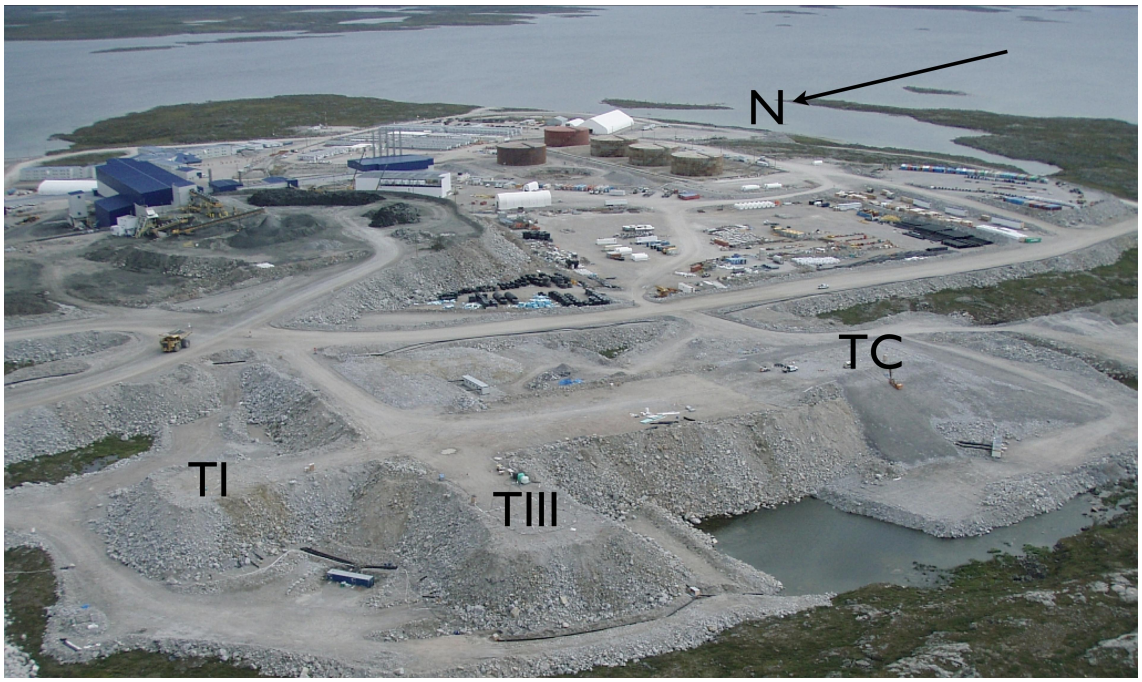

Figure 1.3: Aerial shot of the Diavik waste rock test piles [10].

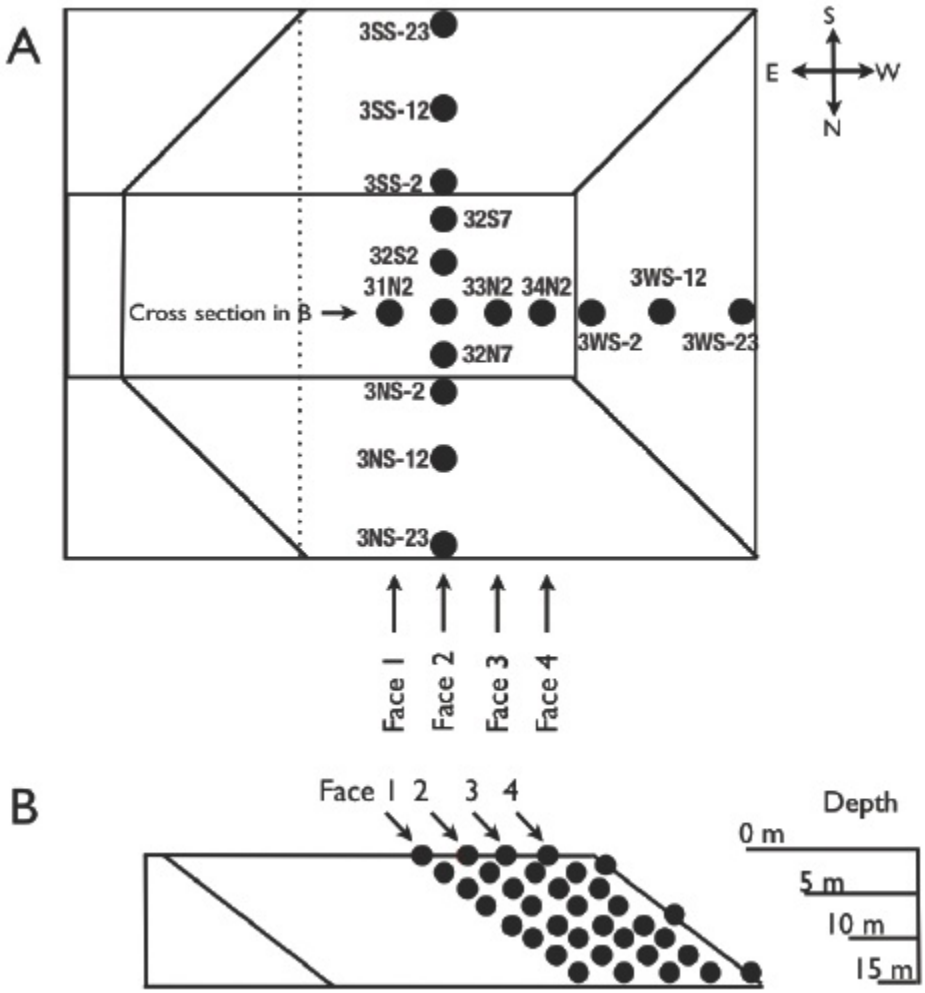

Figure 1.4: Schematic of the test pile geometry. The black dots indicate pressure measurement sampling points. A) The top-down view of the pile. B) The cross-section along the line of sampling points indicated in A [10].

of heat [16]. In general, the rate of reaction is defined by the expression

$$\dot{\xi} = \frac{\partial \xi}{\partial t} \equiv \frac{1}{\nu_i} \frac{\partial n_i}{\partial t} \tag{1.2}$$

where ξ is the extent of the reaction, ν_i is the stoichiometric coefficient of a given substance X_i in the reaction, and n_i is the amount of X_i in the system, often given in units of moles or concentration. The extent of reaction is defined relative to some arbitrary initial point as

$$n_i = (n_i)_0 + \nu_i \xi, \tag{1.3}$$

and is independent of the choice of X_i. $\dot{\xi}$ is always taken to be positive, therefore the standard convention is to set ν_i to be negative for reactants, and positive for products, as the amount of reactant and product for the forward reaction are increasing and decreasing, respectively [7]. For sulfide oxidation, the rate can be defined as

$$\dot{\xi} = -\frac{1}{2}\frac{\partial n_{FeS_2}}{\partial t} = -\frac{1}{7}\frac{\partial n_{O_2}}{\partial t} = -\frac{1}{2}\frac{\partial n_{H_2O}}{\partial t} = \frac{1}{2}\frac{\partial n_{Fe^{2+}}}{\partial t} = \frac{1}{4}\frac{\partial n_{SO_4^{2-}}}{\partial t} = \frac{1}{4}\frac{\partial n_{H^+}}{\partial t}. \tag{1.4}$$

Reaction rate is also often defined in terms of an empirical rate expression. For a reaction taking place in a single step, this is given as

$$\dot{\xi} = k[X_1]^{\alpha_1}[X_2]^{\alpha_2} \cdots [X_n]^{\alpha_n}, \tag{1.5}$$

where k is the empirically determined rate constant and the α_i are derived experimentally.

In general, there are several factors that influence reaction rate. Increases in concentration and pressure result in an increase in the amount of reactants present in a given volume of space, increasing the likelihood of the collisions between particles required for the reaction. Higher temperatures imply more kinetic energy in the system, also increasing collision probability. The dependence of reaction rate on temperature is demonstrated by the Arrhenius equation,

$$k = Ae^{-E_a/RT}. \tag{1.6}$$

This is an empirical relationship, where k is the rate constant of the reaction, A is an experimentally determined pre-exponential factor dependent on the reaction, T is the temperature, R is the ideal gas constant, and E_a is the reaction's energy of activation [7]. Activation energy is the energy that a reaction must overcome in order to take place, and is therefore generally positive, except in certain barrierless reactions. For sulfide oxidation, E_a has been observed to vary from 34 kJ/mol to 121.1 kJ/mol across a range of temperatures and pH levels [22].

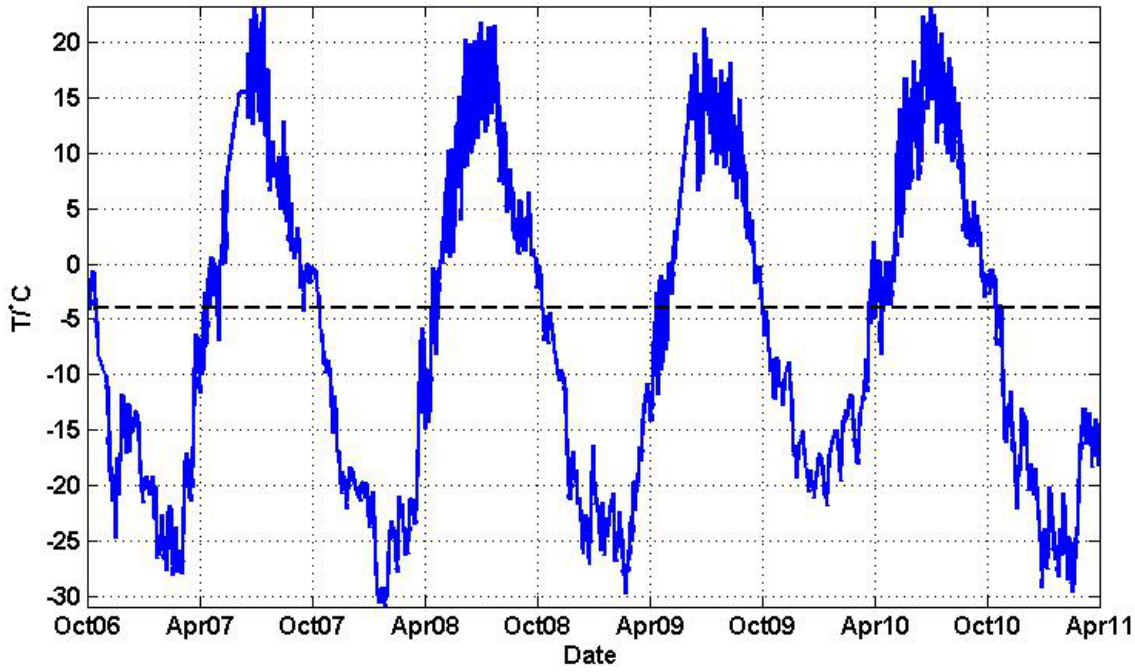

Figure 1.5: Surface temperature for the Diavik Diamond Mine from October 2006 to April 2011 (solid line). The dashed line represents the average temperature over this period.

In waste rock piles, sulfide oxidation is further dependent on a number of other different processes. Gas transport is responsible for supplying the oxygen required for the reaction. Water flow supplies one of the main reactants for sulfide oxidation, and is responsible for reaction product transport. Thermal transport determines the phase of water in piles, and because of the subzero temperatures prevalent in the Northwest Territories, reduces its availability for reaction due to freezing. This may be an important limiting step in AMD, as it both limits the amount of reactant available and prevents flow for the transport of acid [10]. Figure 1.5 presents the surface temperature profile for the Diavik Mine site from October 2006 to April 2011. For most of the year, the temperature of the site is below 0°C. Geochemistry determines the amount of substance available for reaction and acid production. Waste rock at the Diavik site in particular is classified into three different groups of varying sulfur content and acid generating potential [10].

Due to its geographical location, Northern Canada experiences several interesting climatic phenomena [14]. Because of the axial tilt of the Earth and the high northern latitude of the region, the area experiences extremely extended summer daylight hours. Some areas

north of 65.5°N experience periods of 24 hours of daylight centred around June 21, while communities located further to the South, like Fort Smith experience up to 18.9 hours of daylight per day. Regions above 67.5°N will experience extended periods of zero daylight. For example, in Fort Smith the sun will set around November 15, and not rise again until around January 26. The hours of daylight (when the sun is still above the horizon), twilight, or, as it is called in Figure 1.6, skylight (the point at which the sun is below the horizon but still gives light), and total illumination for Fort Smith, NWT (60°N), Sachs Harbour, NWT (72°N), and Dawson, Yukon (64°N) are presented in Figure 1.6. In the absence of cold air intrusions, these longer periods of daylight in June and July tend to result in relatively high temperatures into the evening and night. The resulting high temperatures can lead to thundershowers in the late evening or after midnight. The region's bodies of water are also subjected to earlier freeze-up times and later break-up times than most of the country. From 1988-1998, the Back Bay area of Great Slave Lake near Yellowknife experienced early, median and late freeze-up dates of October 18, October 28, and November 18, respectively. It also experienced early, median and late break-up dates of May 28, June 1, and June 5, respectively. The upper atmospheric flow in this region is controlled by two key factors. The first is the Aleutian Low/Pacific High. The second is a low pressure region that, on average, is located near the centre of the Alaskan Islands in the summer, and becomes more intense and moves closer to Foxe Basin in the winter. During the winter, the mean flow tends to be significantly stronger than in the summer, and originates from a more northwesterly direction, while during the summer, the flow tends to originate more from the west. Mean flow patterns for the summer and winter are displayed in Figures 1.7 and 1.8, respectively [14].

1.2 Flow in Porous Media

1.2.1 Darcy's Law

At the core of the study of porous media flow is Darcy's law, the constitutive equation proposed by Henry Darcy in 1856. Based on his experiments in unidirectional steady-state flow through a uniform porous medium, he observed a proportionality relationship between rate of flow, u, and applied pressure gradient [20]. The one-dimensional equation is given by

$$u = -\frac{K}{\mu}\frac{\partial p}{\partial x}, \tag{1.7}$$

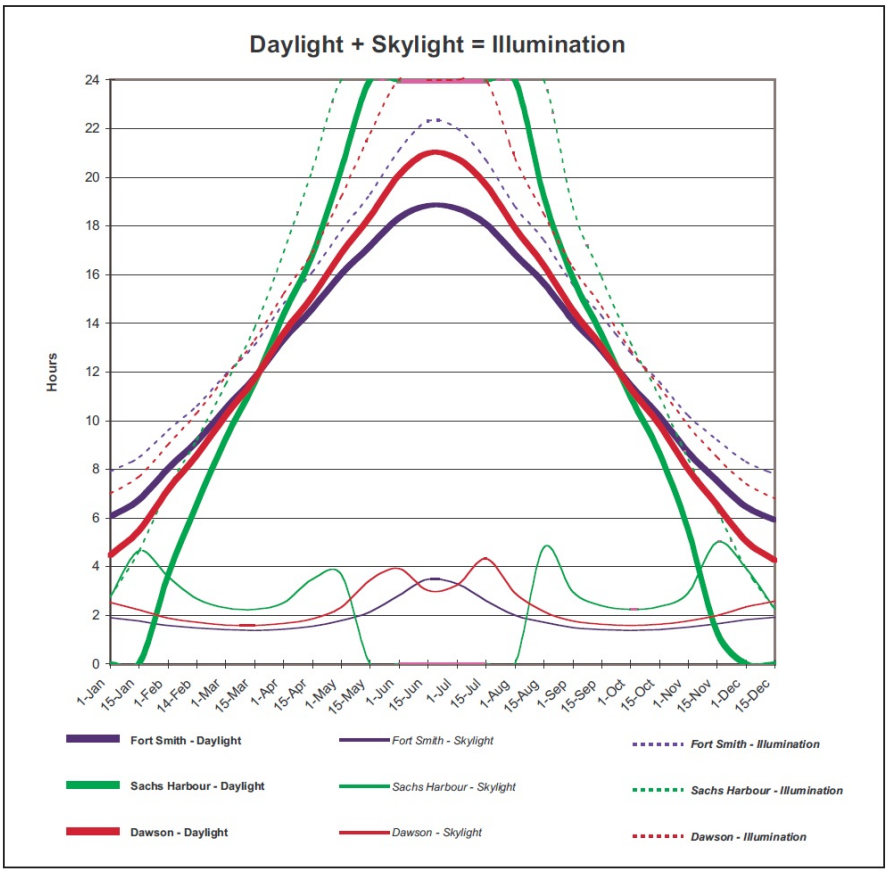

Figure 1.6: Periods of daylight (thick line), skylight (thin line), and total illumination (dashed line) for Fort Smith, Sachs Harbour and Dawson [14].

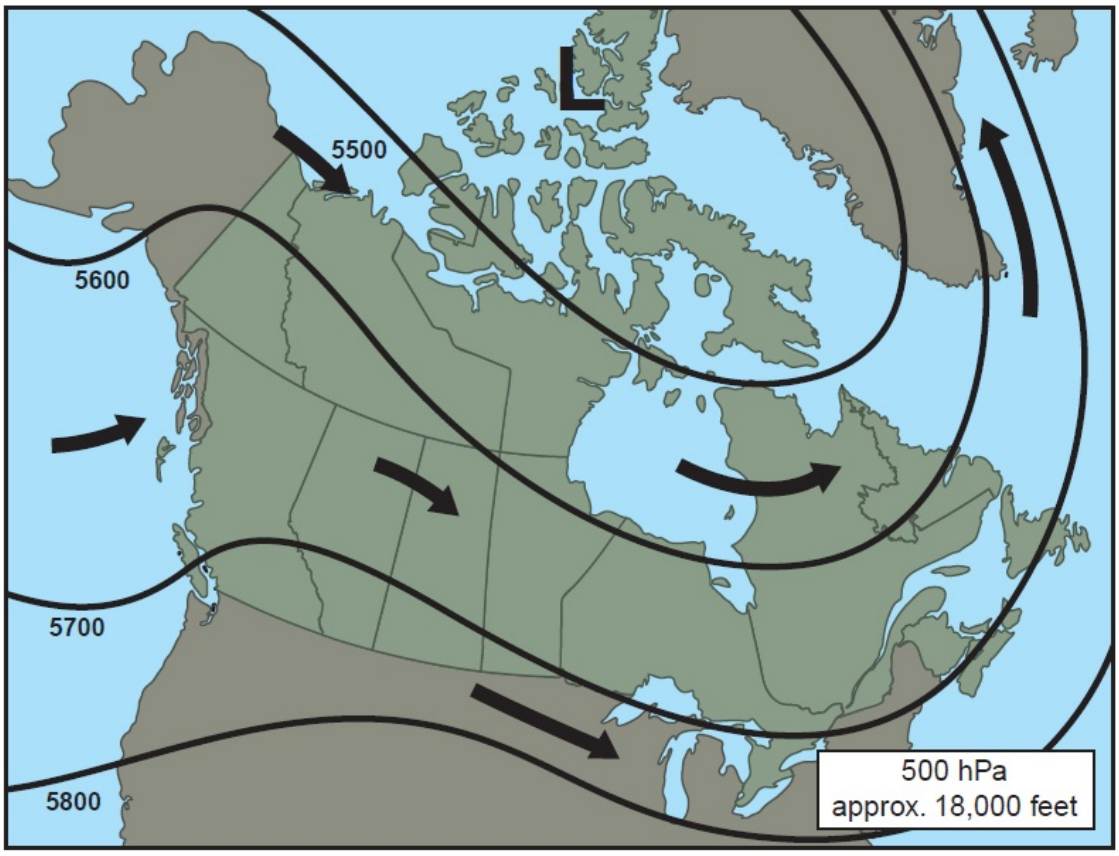

Figure 1.7: The mean upper winds across Canada during the summer at a height of approximately 18000 feet [14].

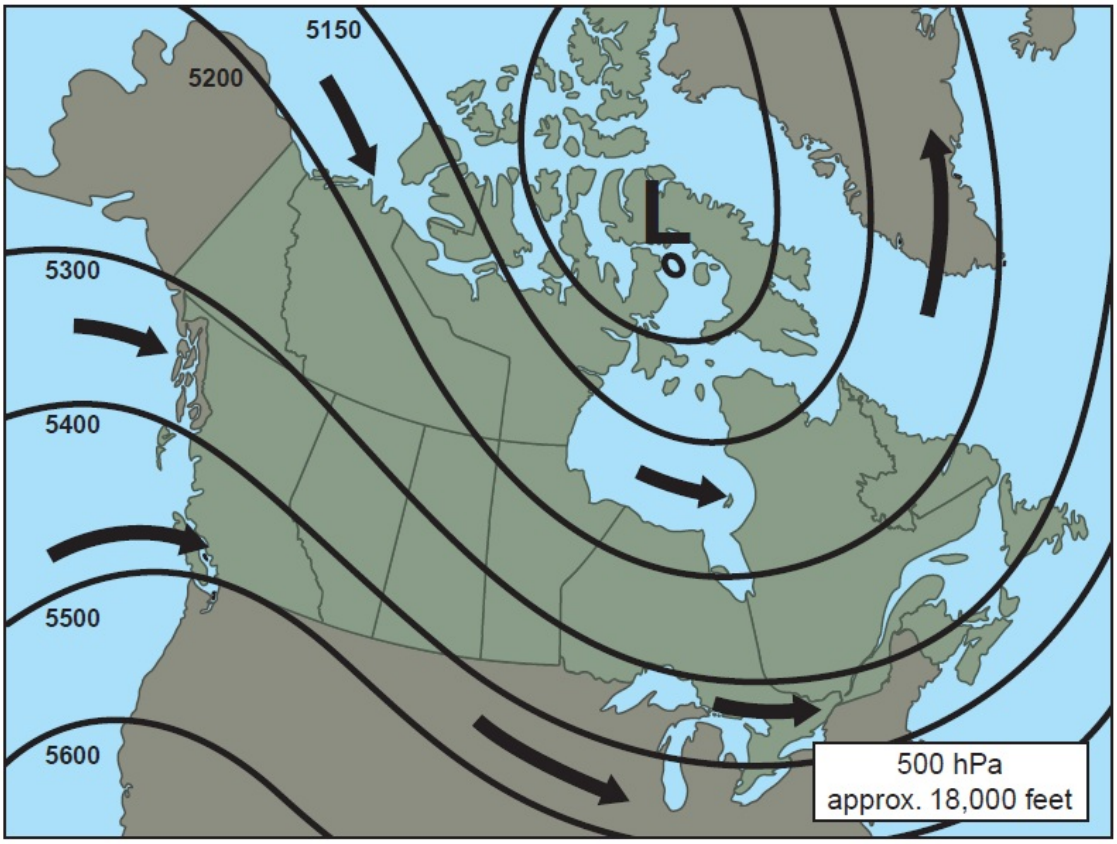

Figure 1.8: The mean upper winds across Canada during the winter at a height of approximately 18000 feet [14].

where p is the applied pressure, and μ is the fluid's dynamic viscosity. K is the specific permeability, a value dependent on the geometry of the porous medium with units of length squared. In an isotropic medium, that is, a material with identical properties in all directions, the generalization of Darcy's law to three dimensions is

$$\boldsymbol{u} = -\frac{K}{\mu}\nabla p, \tag{1.8}$$

which is generally valid for a slowly moving, viscous fluid. It is also common for a buoyancy term to be included on the right side of this equation. Other common forms of (1.8) include the addition of a quadratic drag term in cases of non-negligible inertial forces (Forchheimer's equation), and the addition of another viscous term similar to the Laplacian term appearing in the Navier-Stokes equation (Brinkman's equation), which is important for situations involving shear stress [20].

It is important to understand the domain on which Darcy's law remains valid. As in Figure 1.9, L is defined as the characteristic length scale for the macroscopic domain of interest, while l is the length scale characteristic of the fluid filled pores. Porosity ϕ is a dimensionless quantity defined as the fraction by volume of a porous medium occupied by empty space. The fraction of solid material occupying the total volume of a porous medium is therefore given by $1 - \phi$. This definition of porosity is made under the assumption that this void space is completely saturated by the fluid, and that there is complete interconnectedness for both the solid and fluid components. When permeability is constant, for scales on the order of L, it can be assumed that the medium is homogeneous, and that Darcy's law holds on these scales. For length scales on the order of l, the medium will not be homogeneous, and the domain will be almost entirely solid or fluid material. In these regions, Darcy's law will not be applicable. If these small scale regions are fluid-filled, the Navier-Stokes equation, albeit possibly on a very complicated domain, would be more applicable. In real porous media, permeability is rarely constant. In natural material, particulate matter can vary in size by several orders of magnitude. In waste rock, length scales tend to range from millimetres to metres. For example, in the Diavik waste rock test piles, using digital image processing, permeability was found to range between 10^{-11} m^2 to 10^{-7} m^2 and 10^{-12} m^2 to 10^{-8} m^2 depending on the empirical formula used [10]. Variable permeability distributions can have a significant effect on fluid flow. Therefore, it would be beneficial to develop a model that can simulate a wide range of permeabilities with specific geometric distributions.

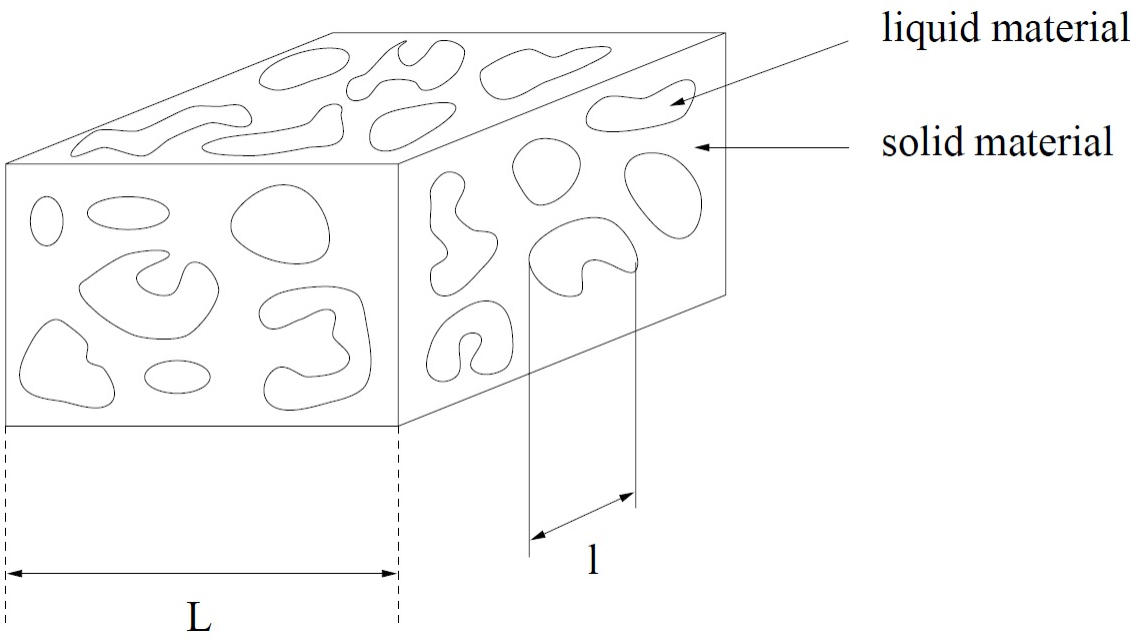

Figure 1.9: Diagram of a sample of porous material, where L represents the macroscopic length scale characteristic of the entire domain, and l represents the much smaller characteristic length scale of the fluid-filled voids [24].

1.2.2 A Brief Review of Previous Models

Although low permeability covers have been shown to significantly reduce oxygen levels and reduce pyrite oxidation rates in waste rock piles [12], pile cover construction can be expensive and time consuming process. Alternatively, it may be possible to obtain satisfactory results by building piles in such a way that oxygen flow is limited using various types of waste rock already on site. Thus, the development of a model to determine ideal pile construction is important to ensure cost-effectiveness and an appropriate use of resources.

In waste rock piles, heat transport, oxygen supply and oxygen reaction form a feedback loop. Because of the exothermic nature of the oxidation reaction, more heat is produced in the pile, raising the pile's temperature and encouraging convection, which supplies more oxygen for the reaction. Similarly, the consumption of oxygen by the reaction removes oxygen from the pile and causes a gradient in oxygen concentration, resulting in more oxygen being supplied by diffusion. A thorough qualitative discussion of the relative influences of external and internal conditions on mass, fluid, and heat transfer processes in the pile can be found in [16]. By examining temperature and oxygen profiles for different piles, Lefebvre et al. were able to infer the processes that control gas transport in each pile [16]. However, this paper simplifies Darcy's law to be dependent on a buoyancy term only, and removes the pressure gradient term. The assumption is justified by arguing that the infiltrating water is at atmospheric pressure, and thus there is no pressure gradient.

TOUGH AMD is a numerical computation program designed to model the multi-physics problem of acid mine drainage. The model accounts for numerous physical properties, including multiphase flow, heat transfer, gaseous diffusion, pyrite oxidation kinetics, and dissolved mass transport. It discretizes in space by using a so-called integral finite difference scheme, and the Newton-Raphson technique for iteratively solving a system of non-linear coupled equations [17]. As mentioned above, however, the model does make the assumption that water infiltrating the pile is at atmospheric pressure, and thus Darcy's law depends only on the buoyancy term and not the pressure gradient [16]. In the second of two 2001 papers, Lefebvre et al. used TOUGH AMD to model transport in two well-characterized waste rock piles of differing physical properties. Additionally, methods to reduce acid mine drainage (AMD) from the piles were also investigated numerically.

Anne and Pantelis [1] attempted to couple a computational fluid dynamics (CFD) model of flow and pressure distribution around a pile with a heat and mass transfer model in a heap of oxidizable material in order to simulate wind-driven porous media flow. Their code computed "the steady-state, incompressible, turbulent flow around the heap" using a k-ϵ model to use as boundary conditions. This type of model is called a two-equation

model, which solves transport equations for two different turbulence variables (in this case, turbulent kinetic energy, k, and turbulent dissipation, ϵ). Using typical physical parameters, flow through a constant permeability trapezoidal heap was computed. Flow was modeled both in a static atmosphere with oxidation and heat generation in the heap, and under the influence of a prevailing wind without oxidation or heat generation. The k-ϵ model is an example of a Reynolds averaged model, or RANS, and thus cannot model the detailed turbulent processes around the pile. Moreover, the k-ϵ model generally requires additional considerations in the boundary layer, and thus this does not seem like an ideal manner in which to pursue the problem of flow over a pile.

Another numerical model used in simulation of waste rock piles is FIDHELM, which is a finite difference model developed by the Australian Nuclear Science and Technology Organization (ANSTO) for modeling heap leaching. It is similar to TOUGH AMD in that in a two-dimensional domain simulating a porous pile of oxidizable material, it couples the physics of gas, heat and water flow. Bennett et al. used this model to simulate flow through a waste rock pile at the Heath Steele Mine in New Brunswick, using measurements from the site as input data for the model [5]. The computational domain in this study was a truncated cone in cylindrical coordinates. The model did not permit any heterogeneity in the pile's physical and material properties, which means that the permeability was held constant. Boundary conditions were independent of space and time. These efforts were unsuccessful in reproducing the measured oxygen contours in the pile.

In his 2010 Master's thesis [10], Chi focused on characterizing gas transport through the Diavik test waste rock piles. Pressure was measured at various points throughout a pile's interior and on its surface. Wind speed and direction across the mine site were recorded. A linear relationship between surface and internal pressure measurements was observed, which suggested the flow through the waste pile obeyed Darcy's law. Dominant wind periods were shown to range from 1 to 50 days using spectral analysis. Wind vectors were measured and broken down into their component north, south, east, and west vectors. Calculation of the correlation between each of the component vectors and the surface pressure measurements of the piles showed the that the highest correlation was obtained by the north component of the wind (mildly to strongly correlated), followed by the south component (mildly to strongly correlated), then the west and east components (weakly correlated). Correlations between pressure measurements in the pile's interior and the wind vectors were generally found to be weaker than the correlations between wind vectors and the surface pressure measurements.

The presence of certain bacteria in waste rock piles may also catalyze pyrite oxidation, however this is outside the scope of this thesis.

As previously mentioned, the freezing of water in the subzero temperatures of the Diavik Mine site may play an important role in the oxidation of sulfides. It is entirely possible that the water in the waste rock piles remains frozen for most, if not all of the year, and that the heat produced by the exothermic oxidation reaction is unimportant in driving gas transport. If this is the case, pressure and wind driven flow may become the main factors in driving gas transport, which would require further examination. In this thesis, the purely pressure driven flow of air through a porous cylinder with varying permeability obeying Darcy's law is examined. The mathematical concepts and techniques used in developing the model are presented, as well as the basics of pseudo-spectral numerical modeling for partial differential equations. Steady-state simulations of incompressible flow and unsteady simulations of slightly compressible flow are presented and discussed. These steady results are compared to a finite element method model that simulates pressure driven flow on a domain more representative of the waste rock piles. The work is not meant to "compete" with the more complete engineering type models, such as TOUGH AMD [16][17] and FIDHELM [5], but is instead intended as the simplest rational model available for wind driven process in the presence of turbulence. Moreover, the pseudo-spectral techniques used can serve as the "gold standard" for future simulations.

Chapter 2

Methodology

In this thesis, several numerical and analytical techniques are applied to study the modeling of porous media flow. These mathematical concepts and techniques are presented and discussed in this chapter.

2.1 Fourier Series

This discussion of Fourier series follows the description of Fourier series in Haberman's *Applied Partial Differential Equations* [11]. For the function $f(x)$ on the interval $-L \leq x \leq L$, its Fourier series is the infinite sum of sines and cosines,

$$a_0 + \sum_{n=1}^{\infty} a_n \cos\left(\frac{n\pi x}{L}\right) + \sum_{n=1}^{\infty} b_n \sin\left(\frac{n\pi x}{L}\right), \tag{2.1}$$

where the coefficients a_0, a_n, and b_n are given by

$$a_0 = \frac{1}{2L}\int_{-L}^{L} f(x)\, dx, \tag{2.2}$$

$$a_n = \frac{1}{L}\int_{-L}^{L} f(x) \cos\left(\frac{n\pi x}{L}\right) dx, \tag{2.3}$$

$$b_n = \frac{1}{L}\int_{-L}^{L} f(x) \sin\left(\frac{n\pi x}{L}\right) dx. \tag{2.4}$$

(2.1) represents $f(x)$ as a series of oscillating functions of different frequencies, or wave numbers in space. The existence of a Fourier series requires the existence of a_0, or that $\left|\int_{-L}^{L} f(x)\,dx\right| < \infty$. The existence of a_0, however, does not guarantee the convergence of the infinite series. When (2.1) converges to the function $f(x)$, the notation

$$f(x) \sim a_0 + \sum_{n=1}^{\infty} a_n \cos\left(\frac{n\pi x}{L}\right) + \sum_{n=1}^{infty} b_n \sin\left(\frac{n\pi x}{L}\right) \tag{2.5}$$

is used. Whether a Fourier series will converge to a given function or not is determined by Fourier's theorem:

Theorem 2.1.1. (Fourier's Theorem) *If a function $f(x)$ is piecewise smooth on the interval $-L \leq x \leq L$, then its Fourier series converges to the periodic extension of $f(x)$.*

When computing the Fourier coefficients of a function $f(x)$, the procedure can be simplified based on the nature of the function. If $f(x)$ is even, b_n will be zero, since the integrand in (2.4) will be odd, and the integral of an odd function over a symmetric interval is zero. Similarly, if $f(x)$ is odd, then both a_0 and a_n will be zero. Therefore, the Fourier series of even and odd functions will be given by the infinite series of even and odd functions

$$f(x) \sim a_0 + \sum_{n=1}^{\infty} a_n \cos\left(\frac{n\pi x}{L}\right), \tag{2.6}$$

and

$$f(x) \sim \sum_{n=1}^{\infty} b_n \sin\left(\frac{n\pi x}{L}\right), \tag{2.7}$$

respectively. From this, the even and odd extensions of a general function can be defined. If $f(x)$ is some function defined on $0 \leq x \leq L$ that is not necessarily even or odd, it can be extended as an even or odd function on $-L \leq x \leq L$. The even extension of $f(x)$ is composed only of cosines, and is given by

$$f_E(x) \sim \sum_{n=0}^{\infty} A_n \cos\left(\frac{n\pi x}{L}\right), \quad -L \leq x \leq L, \tag{2.8}$$

where

$$A_0 = \frac{1}{L}\int_{-L}^{L} f(x)\,dx, \tag{2.9}$$

$$A_n = \frac{2}{L}\int_{-L}^{L} f(x)\cos\left(\frac{n\pi x}{L}\right)dx. \tag{2.10}$$

The odd extension of $f(x)$ is composed only of sines, and is given by

$$f_O(x) \sim \sum_{n=1}^{\infty} B_n \sin\left(\frac{n\pi x}{L}\right), \quad -L \le x \le L, \tag{2.11}$$

where

$$B_n = \frac{2}{L}\int_{0}^{L} f(x)\sin\left(\frac{n\pi x}{L}\right)dx. \tag{2.12}$$

In practice, it is often useful to approximate complicated functions using finite Fourier series. Even and odd functions are also useful when designing functions with desired properties. One can build a function composed of various other functions on a smaller domain (e.g., trigonometric functions, polynomials), then extend the function to be even or odd on a larger domain. This application of Fourier series is implemented later in this thesis.

2.2 Fourier Transforms

This discussion on the Fourier transform and the Chebyshev method follow from Trefethen's book *Spectral Methods in Matlab* [25]. The Fourier transform of a function in terms of the physical variable x to the Fourier variable or wave number, k, is given by the formula

$$\hat{u}(k) = \mathcal{F}\{u(x)\} = \int_{-\infty}^{\infty} e^{-ikx}u(x)\,dx, \quad k \in \mathbb{R}, \tag{2.13}$$

where $\hat{u}(k)$ can be considered the amplitude density in terms of k. By applying the Fourier transform to a function, the function is decomposed into each of its component waves. The inverse Fourier transform,

$$u(x) = \frac{1}{2\pi}\int_{-\infty}^{\infty} e^{ikx}\hat{u}(k)\,dk, \quad x \in \mathbb{R}, \tag{2.14}$$

transforms the function from Fourier space back to physical space, and facilitates the description of the derivatives of u in terms of its Fourier transform. For the νth derivative of u with respect to x, the inverse Fourier transform is given by

$$u^{(\nu)}(x) = \frac{1}{2\pi}\int_{-\infty}^{\infty} (ik)^{\nu} e^{ikx}\hat{u}(k)\,dk. \tag{2.15}$$

This means that the Fourier transform of $u^{(\nu)}(x)$ is given simply by multiplying the Fourier transform of $u(x)$ by $(ik)^{\nu}$.

Fourier transforms have numerous applications in a variety of subjects, such as Fourier transform infrared (FTIR) spectroscopy [3] and digital signal processing [18]. In this thesis, however, special attention is paid to their ability to convert partial differential equations into ordinary differential equations, and their use in spectral and pseudo-spectral methods for numerical computation. In particular, the fact that the Fourier transform of a periodic function reduces to a Fourier series motivates the consideration of the discrete Fourier transform.

2.2.1 Numerical Differentiation with Fourier Transforms

When dealing with numerical computation, instead of the infinite continuous domain $\mathbb{R}$, x needs to be considered over a finite discrete grid. As per [25], during this discussion, the number of grid points on the periodic grid, N, will be kept even, and the domain will be restricted to $[0, 2\pi]$, although the scaling and transformation to other domains is straightforward. The grid spacing is given by $\Delta x = 2\pi/N$. For $v_j = u(x_j)$, where x_j is the grid point in $[0, 2\pi]$ such that $x_j = j\Delta x = \frac{2\pi}{N}$, the discrete Fourier transform (DFT) takes the form

$$\hat{v}_k = \Delta x \sum_{j=1}^{N} e^{-ikx_j} v_j, \quad k = -\frac{N}{2} + 1, \ldots, \frac{N}{2}. \tag{2.16}$$

The inverse discrete Fourier transform is

$$v_j = \frac{1}{2\pi} \sum_{k=-N/2+1}^{N/2} e^{ikx_j} \hat{v}_k, \quad j = 1, \ldots, N. \tag{2.17}$$

When applying spectral differentiation to a function u, one approach is to interpolate the grid function v using a continuous function p that is readily differentiable such that $p(x_j) = v_j$. One way is to determine the band-limited interpolant, that is, the interpolant with compact support limited to a given interval, of the periodic Kronecker delta function,

$$\delta_j = \begin{cases} 1, & j \equiv 0 \,(\mathrm{mod}\, N), \\ 0, & j \not\equiv 0 \,(\mathrm{mod}\, N), \end{cases}$$

and express the grid function as a linear combination of these functions,

$$v_j = \sum_{m=1}^{N} v_m \delta_{j-m}. \tag{2.18}$$

As per [25], the band-limited interpolant of δ_j is determined to be the periodic sinc function

$$S_N(x) = \frac{\sin(\pi x/\Delta x)}{(2\pi/\Delta x)\tan(x/2)}. \tag{2.19}$$

The continuous differentiable interpolant of the grid function is then given by

$$p(x) = \sum_{m=1}^{N} v_m S_N(x - x_m). \tag{2.20}$$

The derivatives of v are computed by differentiating $p(x)$, so that the νth derivative of v is

$$p^{(\nu)}(x) = \sum_{m=1}^{N} v_m S_N^{(\nu)}(x - x_m). \tag{2.21}$$

The discrete derivative of the grid function is then denoted by w, where $p'(x_j) = w_j$. Since the grid function and its derivative are evaluated on a discrete set of points, their relationship can be expressed through matrix-vector multiplication,

$$\boldsymbol{w} = D_N \boldsymbol{v}, \tag{2.22}$$

where $\boldsymbol{v} = (v_1, v_2, \ldots, v_N)^T$ and $\boldsymbol{w} = (w_1, w_2, \ldots, w_N)^T$. D_N is the $N \times N$ differentiation matrix, where the elements of the Nth column are defined by

$$S'_N(x_j) = \begin{cases} 0, & j \equiv 0 \,(\mathrm{mod} N), \\ \frac{1}{2}(-1)^j \cot(j\Delta x/2), & j \not\equiv 0 \,(\mathrm{mod} N). \end{cases}$$

When computing the second derivative of v, the elements of the Nth column of $D_N^{(2)}$ are given by

$$S''_N(x_j) = \begin{cases} -\dfrac{\pi^2}{3\Delta x^2} - \dfrac{1}{6}, & j \equiv 0 \,(\mathrm{mod} N), \\ -\dfrac{(-1)^j}{2\sin^2(j\Delta x/2)}, & j \not\equiv 0 \,(\mathrm{mod} N). \end{cases}$$

The development of the Fast Fourier Transform (FFT) algorithm in 1963 [25] led to the more widespread adoption of an alternative to interpolation. Prior to the discovery of the FFT, this method was generally considered too computationally expensive when compared to other numerical schemes. The first step to this scheme is to perform a DFT on the grid function, $\hat{v} = \mathcal{F}_D\{v\}$. As per (2.15), the components of the derivative of v in Fourier space are given by $\hat{w}_k = ik\hat{v}_k$. The derivative of v in physical space, w, is then returned by performing an inverse FFT on $\hat{w}$, $w = \mathcal{F}_D^{-1}\{\hat{w}\}$.

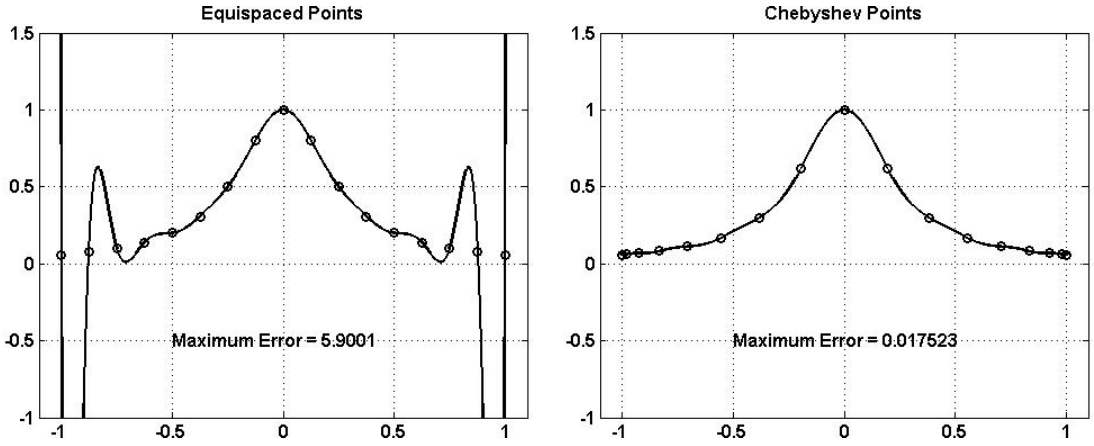

Figure 2.1: Polynomial interpolation of $u(x) = 1/(1+16x^2)$ using (a) equispaced points and (b) Chebyshev points [25].

2.3 Chebyshev Method

While trigonometric polynomial interpolation schemes such as Fourier spectral methods are very well suited to problems on periodic domains (such as the azimuthal direction in cylindrical coordinates), their applicability generally does not extend to non-periodic functions. While the periodic extension of some functions is possible, this is not true in general, since even though a function may be smooth on the domain of interest, its periodic extension will introduce discontinuities if its boundary values differ. The presence of these discontinuities results in global contamination when Fourier spectral methods are applied. This source of error is similar to the Gibbs phenomenon. To avoid Gibbs-like phenomenon on a non-periodic grid, algebraic polynomial interpolation is often used instead of trigonometric polynomial interpolation [25]. When used on a grid of equally spaced points, however, algebraic polynomials can yield even poorer results than trigonometric polynomials due to the Runge phenomenon, as illustrated in Figure 2.1. As per [25], Figure 2.1 displays an attempt to use degree N polynomial interpolation of $u(x) = 1/(1+16x^2)$ with $N+1$ points on an equispaced grid and on a Chebyshev grid (described below), where $N = 16$. The exponential error increase with increasing N in the equispaced case is the Runge phenomenon. There is an exponential decrease in error with increasing N in the case of the Chebyshev grid [25]. The solution is therefore to use algebraic interpolation on an unevenly spaced grid, specifically one where the grid points are concentrated near the boundaries.

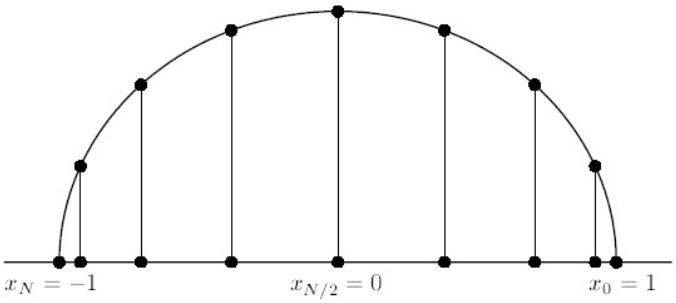

Figure 2.2: The projection of points equispaced along a semi-circle onto the x-axis to create the Chebyshev grid [25].

There are several different grids that are well-suited to this, all of which have the grid point distribution density per unit length of

$$\text{density} \ \sim \frac{N}{\pi\sqrt{1-x^2}} \tag{2.23}$$

as $N \to \infty$. The simplest grid satisfying this density condition is the Chebyshev grid,

$$x_j = \cos\left(j\pi/N\right), \quad j = 0, 1 \ldots N, \tag{2.24}$$

where $N+1$ is the total number of grid points, and N is some positive integer. Geometrically, this is the projection of equally spaced points along the upper half of the unit circle onto the x-axis from -1 to 1. For a grid function v, the discrete derivative w is found through interpolation on the Chebyshev grid by first determining the unique polynomial p with degree less than or equal to N such that $p\left(x_j\right) = v_j$, $0 \leq j \leq N$, and differentiating the polynomial so that $w_j = p'\left(x_j\right)$. This is a linear operation, and as such can be expressed as multiplication by an $N+1 \times N+1$ matrix, D_N,

$$\boldsymbol{w} = D_N \boldsymbol{v}, \tag{2.25}$$

where $\boldsymbol{v} = \left(v_0, v_1, v_2, \ldots, v_N\right)^T$ and $\boldsymbol{w} = \left(w_0, w_1, w_2, \ldots, w_N\right)^T$. With the indices of the rows and columns running from 0 to N, the elements of this differentiation matrix are given by the formulas

$$\left(D_N\right)_{00} = \frac{2N^2+1}{6}, \tag{2.26}$$

$$\left(D_N\right)_{NN} = -\frac{2N^2+1}{6}, \tag{2.27}$$

$$(D_N)_{jj} = \frac{-x_j}{2(1-x_j)}, \quad j = 0, 1 \ldots N, \tag{2.28}$$

$$(D_N)_{jj} = \frac{c_i}{c_j}\frac{(-1)^{i+j}}{(x_i - x_j)}, \quad i \neq j \quad i, j = 0, 1 \ldots N-1, \tag{2.29}$$

where

$$c_i = \begin{cases} 2, & i = 0 \text{ or } N, \\ 1, & \text{otherwise.} \end{cases}$$

Both the Chebyshev grid and differentiation matrix used in this thesis have been generated using the `cheb.m` Matlab function written by Trefethen [25]. For higher order derivatives, the differentiation matrix needs only to be raised to the power equal to the order of the derivative (e.g., $D_N^2 \equiv \frac{\partial^2}{\partial x^2}$).

2.4 Separation of Variables

The separation of variables technique is a common and straightforward approach to solving linear PDEs. This discussion follows from the introduction to the separation of variables technique presented in reference [11]. An operator $\mathcal{L}$ is said to be linear if for any two arbitrary functions, u_1 and u_2,

$$\mathcal{L}\{c_1 u_1 + c_2 u_2\} = c_1 \mathcal{L}\{u_1\} + c_2 \mathcal{L}\{u_2\}, \tag{2.30}$$

for constants c_1 and c_2. A linear equation in terms of u is therefore an equation that takes the form

$$\mathcal{L}\{u\} = f. \tag{2.31}$$

When $f = 0$, (2.31) is referred to as a homogeneous linear equation. For example, for a function $u = u(x,t)$, the one-dimensional linear diffusion equation

$$\frac{\partial u}{\partial t} = k\frac{\partial^2 u}{\partial x^2}, \tag{2.32}$$

where k is a constant, is a homogeneous linear differential equation. In this case,

$$\mathcal{L} = \frac{\partial}{\partial t} - k\frac{\partial^2}{\partial x^2} \tag{2.33}$$

is the linear operator. The separation of variables technique assumes that the solution u takes the product form

$$u(x,t) = \phi(x)\, G(t), \tag{2.34}$$

where ϕ and G are functions of x and t only, respectively. By assuming a product solution, a homogeneous PDE can be converted into a pair of ODEs. It should be noted that this assumption can be extended for equations of several variables, e.g., $u(x_1, x_2, \ldots, x_n) = \phi_1(x_1)\,\phi_2(x_2)\cdots\phi_n(x_n)$. Under the assumption of a product solution, each of the partial derivatives in the linear diffusion equation become

$$\frac{\partial u}{\partial t} = \phi(x)\frac{dG}{dt}, \tag{2.35}$$

$$\frac{\partial^2 u}{\partial x^2} = \frac{d^2\phi}{dx^2}G(t). \tag{2.36}$$

With these new expressions for the partial derivatives, (2.33) can be rewritten as

$$\phi(x)\frac{dG}{dt} = k\frac{d^2\phi}{dx^2}G(t). \tag{2.37}$$

Grouping the functions in terms of x on one side and the functions in terms of t on the other yields

$$\frac{1}{kG}\frac{dG}{dt} = \frac{1}{\phi}\frac{d^2\phi}{dx^2}. \tag{2.38}$$

Since the left hand side of (2.38) is a function of t only and the right hand side is a function of x only, the only way equation (2.38) can hold is if both sides are equal to a constant,

$$\frac{1}{kG}\frac{dG}{dt} = \frac{1}{\phi}\frac{d^2\phi}{dx^2} = -\lambda. \tag{2.39}$$

In (2.39), λ is called the separation constant, and is completely arbitrary. The introduction of the minus sign is standard procedure and is simply a matter of convenience. The ODEs resulting from equation (2.39) are

$$\frac{d^2\phi}{dx^2} = -\lambda\phi \tag{2.40}$$

and

$$\frac{dG}{dt} = -\lambda kG. \tag{2.41}$$

When the boundary conditions of the problem are coupled together with equation (2.40), an ordinary differential boundary value problem (BVP) is obtained. Equations of this type are further discussed in the subsequent section. Coupling equation (2.41) with the initial conditions (ICs) of the problem yields an ordinary differential initial value problem (IVP). Existence and uniqueness of a solution to this IVP are guaranteed by the standard

existence and uniqueness theorem studied in most undergraduate courses on ODEs [8]. In simple cases such as (2.41), the exact solution is given by

$$G(t) = Ce^{-\lambda kt}, \tag{2.42}$$

where C is some constant dependent on the ICs.

2.5 Sturm-Liouville Theory

Equation (2.40), the ordinary differential boundary value problem presented in the previous section, belongs to the class of ODEs known as Sturm-Liouville differential equations. A number of important theorems have been proven for this set of equations [11]. A regular Sturm-Liouville eigenvalue problem is given by the equation

$$\frac{d}{dx}\left(p(x)\frac{d\phi}{dx}\right) + q(x)\phi + \lambda\sigma(x)\phi = 0, \quad a < x < b, \tag{2.43}$$

for which $p(x)$, $q(x)$, and $\sigma(x)$ are real and continuous, and $p > 0$ and $\sigma > 0$ everywhere on $[a, b]$. The boundary conditions must be in the form

$$\beta_1\phi(a) + \beta_2\frac{d\phi}{dx}(a) = 0, \tag{2.44}$$

$$\beta_3\phi(b) + \beta_4\frac{d\phi}{dx}(b) = 0, \tag{2.45}$$

where β_i, $i = 1, 2, 3, 4$ are real-valued constants. For example, in the case of equation (2.40), $p(x) = 1$, $q(x) = 0$, and $\sigma(x) = 1$. Several theorems regarding Sturm-Liouville problems of particular relevance to this thesis are listed below:

Theorem 2.5.1. *The eigenvalues λ are all real.*

Theorem 2.5.2. *There exists infinitely many eigenvalues such that:*

- *there is a smallest eigenvalue, λ_1,*
- $\lambda_1 < \lambda_2 < \ldots < \lambda_n < \lambda_{n+1} < \ldots$,
- *there is no largest eigenvalue,*
- *as $n \to \infty$, $\lambda_n \to \infty$.*

Theorem 2.5.3. *There is a unique eigenfunction $\phi(x)$ corresponding to each eigenvalue λ_n that was exactly $n-1$ zeros on (a,b).*

Theorem 2.5.4. *Relative to the weight function $\sigma(x)$, eigenfunctions corresponding to different eigenvalues are orthogonal.*

For cases in which the Sturm-Liouville problem is not regular, some of these theorems may still hold. An example of such problem for which $p = \sigma = 0$ somewhere on the domain is examined in Chapter 4.

2.6 Finite Element Methods

This section presents a short discussion on finite element methods. The important details of this discussion can be found in Haberman's *Applied Partial Differential Equations* [11] and Matlab's *Partial Differential Equation Toolbox User's Guide* [19], which contain good brief introductions to the topic. A more thorough theoretical discussion is presented in *Finite Element Solution of Boundary Value Problems: Theory and Computation* by Axelsson and Barker [2]. The strength of finite element methods is that they allow problems to be solved on irregular geometries that other methods cannot handle or that cannot be obtained using mapped coordinates. The basic idea is to approximate the domain, Ω, using simple geometric elements, generally triangles, and approximate the solution across the domain using a linear combination of basis functions, called test functions. The collection of elements over the domain is called the mesh, while the points at which the corners of these elements meet are called the nodes. A sample finite element mesh is presented in Figure 2.3. When triangular elements are being used, it should be noted that a mesh should not have any hanging nodes, such as in Figure 2.4, where the centre node occupies the side of one of the triangles [6]. Theories with so-called non-conforming elements have been developed, however, but are beyond the scope of the present discussion.

The general procedure for FEMs will be demonstrated in the Cartesian plane using the elliptic problem

$$-\nabla \cdot (c\nabla u) + qu = f, \tag{2.46}$$

where c, q and f are functions of x and y, and u is the scalar function for which the problem is being solved. As described in the next chapter, for a steady-state incompressible flow in a porous medium, $c = \tilde{K}$, $q = f = 0$, and $u = P$. For the sake of this discussion, q is set to zero.

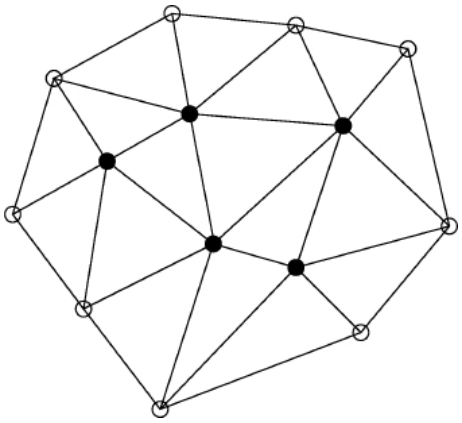

Figure 2.3: A valid computational finite element mesh. The nodes along the boundary are indicated by the circles while the internal nodes are indicated by the black dots [6].

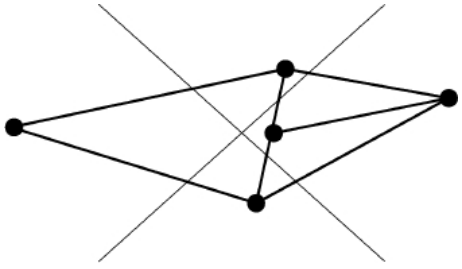

Figure 2.4: An "invalid" finite element mesh with a hanging node [6].

A numerical solution to the PDE is determined by examining an approximation to the solution $U(x,y)$, where U is a linear combination of the test functions $v_j(x,y)$ is

$$U(x,y) = \sum_{j=1}^{n} U_j v_j(x,y). \tag{2.47}$$

Since U is merely an approximation to the solution of (2.46), it is not expected to satisfy that equation exactly. The idea is then to determine the n values of U_j so that (2.47) satisfies the weak form of the PDE. It is assumed that when equation (2.46) with $q = 0$ is multiplied by a test function v_i and integrated over the domain, that the equation

$$\iint_{\Omega} \left(-\nabla \cdot (c\nabla u) - f\right) v_i dA = 0, \tag{2.48}$$

where $dA = dxdy$, still holds. Applying integration by parts to the first term of equation (2.48) yields

$$\iint_{\Omega} \left((c\nabla u) \cdot \nabla v_i\right) dA - \oint_{\partial\Omega} (c\nabla u)\, v_i \cdot \hat{n} ds = \iint_{\Omega} f v_i dA. \tag{2.49}$$

Boundary conditions for this problem are defined in two ways. For Dirichlet conditions where the value of u on the boundary $\partial\Omega$ is known, the v_j are required to be 0. These are called essential boundary conditions, since they must be imposed explicitly by the user. From a theoretical point of view, the approximation space to which v_i belongs is restricted [2]. In practice, these conditions are imposed by modifying the stiffness matrix and the load vector (described below). If Neumann boundary conditions are defined such that $(c\nabla u) \cdot \hat{n} = g$, where g is a function of x and y, then equation (2.49) becomes

$$\iint_{\Omega} \left((c\nabla u) \cdot \nabla v_i\right) dA = \iint_{\Omega} f v_i dA + \oint_{\partial\Omega_N} g v_i ds, \tag{2.50}$$

where $\partial\Omega_N$ is the section of the boundary for which Neumann conditions are defined. It should be noted that the v_i are zero on the portion of the boundary $\partial\Omega - \partial\Omega_N$. Replacing u with the approximation U gives

$$\sum_{j=1}^{n} U_j \left(\iint_{\Omega} \left((c\nabla v_j) \cdot \nabla v_i\right) dA \right) = \iint_{\Omega} f v_i dA + \oint_{\partial\Omega_N} g v_i ds. \tag{2.51}$$

This results in a system of n equations for n unknowns U_j,

$$\sum_{j=1}^{n} K_{ij} U_j = F_i + G_i, \tag{2.52}$$

such that

$$K_{ij} = K_{ji} = \iint_{\Omega} (c \nabla v_j) \cdot \nabla v_i dA, \tag{2.53}$$

$$F_i = \iint_{\Omega} f v_i dA, \tag{2.54}$$

and

$$G_i = \oint_{\partial \Omega_N} g v_i ds. \tag{2.55}$$

The Neumann boundary terms will only be added to those elements of the vector representing the boundary nodes. This can be represented in the matrix form

$$K\boldsymbol{U} = \boldsymbol{F} + \boldsymbol{G}, \tag{2.56}$$

where K is called the stiffness matrix and $\boldsymbol{U}$ is the vector of the values of U_j. $\boldsymbol{F}$ is called the load vector and $\boldsymbol{G}$ corresponds to the boundary values g in the Neumann conditions. For the Dirichlet conditions, the appropriate rows are set to zero, except for the diagonal entry, which is set to 1, while the corresponding entry of the load vector is set to the value of the boundary condition.

The test functions v_i can be chosen in a number of different ways, with the standard being to fit a polynomial to several different nodes. The easiest such function is to use linear "tent" functions, v_i, chosen to be 1 at the ith node, and zero at all other nodes. On a two-dimension mesh, the linear basis functions at the ith node are defined such that

$$v_i(\boldsymbol{x}_j) = \begin{cases} 1, & j = i, \\ 0, & j \neq i. \end{cases}$$

In practice, these basis functions are defined on the standard triangle with vertices and then mapped via a linear mapping to any triangle in the mesh.

In the case where the PDE exhibits time dependence, such as

$$d\frac{\partial u}{\partial t} - \nabla \cdot (c \nabla u) + qu = f, \tag{2.57}$$

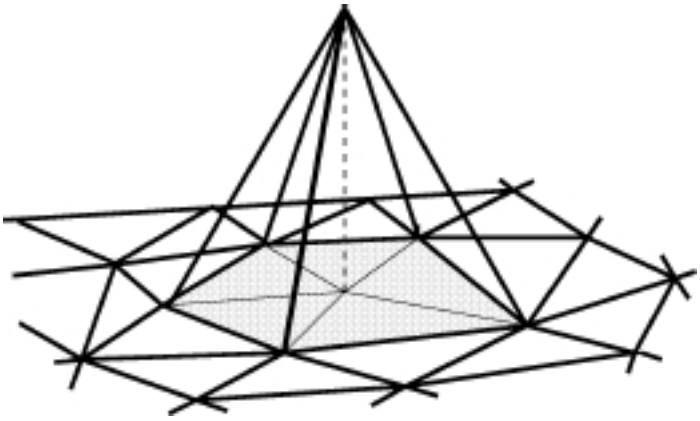

Figure 2.5: Linear basis function v_i equal to 1 at the ith node, and 0 at all other nodes on a mesh of triangular elements [6].

where d, q, a, and f are functions of x, y and t, the problem is solved by making the U_j functions of t such that

$$U(x, y, t) = \sum_{j=1}^{n} U_j(t)\, v_j(x, y). \tag{2.58}$$

Determining the solution through this approach is called the method of lines.

2.7 The Numerical Scheme

The numerical pressure solver used in this thesis to solve for flow of an incompressible fluid governed by Darcy's law inside a porous disc uses the discrete Fourier transform (or equivalently the Fourier series) to transform the dependence along the angular domain into the Fourier domain. As will be discussed in more detail in Chapter 3, in an isotropic medium with a permeability given as a function of $\tilde{r}$, the nondimensionalized form of Darcy's law combined with incompressibility yields the diffusion equation

$$0 = \left(\frac{\partial \tilde{K}}{\partial \tilde{r}} + \frac{\tilde{K}}{\tilde{r}}\right)\frac{\partial P}{\partial \tilde{r}} + \tilde{K}\frac{\partial^2 P}{\partial \tilde{r}^2} + \frac{\tilde{K}}{\tilde{r}^2}\frac{\partial^2 P}{\partial \theta^2}. \tag{2.59}$$

Taking the Fast Fourier Transform of this equation, where $\hat{P}(\tilde{r},k) = \mathcal{F}\{P(\tilde{r},\theta)\}$, and k is the wave number results in

$$0 = \left(\frac{\partial \tilde{K}}{\partial \tilde{r}} + \frac{\tilde{K}}{\tilde{r}}\right)\frac{\partial \hat{P}}{\partial \tilde{r}} + \tilde{K}\frac{\partial^2 \hat{P}}{\partial \tilde{r}^2} - k^2\frac{\tilde{K}}{\tilde{r}^2}\hat{P}. \tag{2.60}$$

Once converted to this form, an ordinary differential equation for each of the individual wave numbers can be solved in terms of $\tilde{r}$. These ODEs are solved numerically using the aforementioned Chebyshev scheme before an IFFT is performed to transform the angular component back into physical space. In order to accommodate the discontinuity that arises in (2.60) at $\tilde{r} = 0$, the radial domain is defined as $-1 \leq \tilde{r} \leq 1$ and an even number of grid points are used. On this domain, the even number of grid points guarantees $\tilde{r} = 0$ will be skipped at the cost of solving for pressure over the entire disc twice [25].

The pseudo-spectral method requires some care to implement boundary conditions properly. Consider the model problem

$$u_{xx} = f(x)$$

with the corresponding discretized form

$$D_N^2 \boldsymbol{u} = \boldsymbol{f}$$

where vectors are the functions evaluated on a Chebyshev grid with $N+1$ points, and D_N is the previously described Chebyshev differentiation matrix. For homogeneous Dirichlet conditions, the first and last rows and columns from the D_N^2 matrix can simply be removed and replaced the first and last entry of $\boldsymbol{f}$ with zero. In the case of inhomogeneous boundary conditions, for example $u(-1) = a$ and $u(1) = b$, the first and last rows and columns of D_N^2 are kept, but are set to zero, with the $(1,1)$ element and the $(N+1, N+1)$ element replaced by 1. The first and last elements of $\boldsymbol{f}$ are therefore set to a and b, respectively. For Neumann boundary conditions, the row of D_N^2 corresponding to the Neumann boundary is replaced by the corresponding row of D_N, with the corresponding element in $\boldsymbol{f}$ set equal to the value of the derivative.

The following subsection contains a brief description of the important sections of the Matlab code.

2.7.1 The Code

The selection of code below presents the key portion of the solver used to compute incompressible flow through a porous disc. Once the vector of `Nt` wave numbers, `lsvec`, and the

Dirichlet boundary conditions are transformed into Fourier space (i.e., the vector `myvals`, has been defined), the ODEs in $\tilde{r}$ for each wave number can be solved in the following manner.

```
for ii=1:Nt
  l2=lsvec(ii)^2;

  % this is the 1D problem we want to solve
  myop=diag(kfunc(r))*D2+diag(kfunc(r)./r + kpfunc(r))*D-l2*diag(kfunc(r)./(r.*r));

  % redefine for the Dirichlet BCs
  myop(1,:)=0;
  myop(end,:)=0;
  myop(1,1)=1;
  myop(end,end)=1;
  myrh=zeros(N+1,1);
  myrh(1)=myvals(ii);
  myrh(end)=myvals(ii);

  % solve
  mysol=myop\myrh;

  % store the solution in the appropriate column of mypb
  mypb(:,ii)=mysol;

  % store the theta derivative
  myptb(:,ii)=sqrt(-1)*lsvec(ii)*mysol;

  % store the r derivative
  myprb(:,ii)=D*mysol;

end
```

The discrete operator corresponding to

$$\mathcal{L} = \left(\frac{\partial \tilde{K}}{\partial \tilde{r}} + \frac{\tilde{K}}{\tilde{r}} \right) \frac{\partial}{\partial \tilde{r}} + \tilde{K} \frac{\partial^2}{\partial \tilde{r}^2} - k^2 \frac{\tilde{K}}{\tilde{r}^2} \tag{2.61}$$

is given by `myop`, where `kfunc` and `kpfunc` are the functions representing the permeability as a function of the radial variable and the derivative of the permeability, respectively. `r` is the vector of the radial Chebyshev grid points, where `r(1)=1`, `r(end)=-1`, and `D` and `D2` are the first and second order derivatives in the radial direction defined on the Chebyshev grid by Trefethen's function `cheb.m` [25]. The first and last rows of `myop` are defined to accommodate the inhomogeneous Dirichlet boundary conditions, as described above. `myrh` corresponds to the zero side of equation (2.59), with the first and last elements of the vector being replaced by the boundary condition corresponding to the `ii`th wave number in Fourier space. Using Matlab's direct solver (backslash), `mysol`, the solution in Fourier space corresponding to the `ii`th wave number, is computed using `myop` and `myrh`, and stored in the appropriate column of `mypb`. The angular derivative of the `ii`th component pressure in Fourier space is computed by multiplying `mysol` by `sqrt(-1)*lsvec(ii)`, as described in the section on Fourier methods. The radial derivative in Fourier space is determined by applying `D` to `mysol`. The pressure and its azimuthal and radial derivatives are computed once this loop has ended by taking the real component of the inverse FFT of `mypb`, `myptb`, and `myprb`, respectively.

Chapter 3

Steady Results

The trapezoidal shape of the Diavik waste rock piles dominates the selection of an appropriate numerical model. While finite difference methods (FDMs) have been used in the Earth science and engineering literature, these often have low orders of accuracy. Finite element methods (FEMs) are readily applied to this type of geometry, though they do not appear to have been considered in detail in the literature pertaining to this topic. Finite volume methods, especially modern variants with the cut-cell methodology also appear well suited to this situation, though again the literature does not describe any such models. Using low order models may be satisfactory for gaining an idea of how flow behaves qualitatively (this will be discussed later), especially when using ad hoc models such as TOUGH AMD. However this is somewhat unsatisfying when studying the mathematics behind the flow, and in particular when using the simplest possible rational models as is the aim of this research. The pile geometry is also somewhat uncommon in terms of the flow over the pile, and has not been well examined during past studies of fluid flow either experimentally or using well-tested numerical models. Of course, a pile with a sharp corner can be expected to yield significant fluid separation. It is therefore desirable to examine an obstacle or domain that has been well-characterized over many decades of fluid dynamics research, namely, the cylinder. This chapter presents a discussion of the steady-state results using Darcy's law for a variety of permeability profiles through a porous cylinder and under conditions of turbulent forcing. This then motivates an examination of flow through a porous trapezoidal domain using a finite element method.

3.1 Incompressible Flow

Darcy's law is a constitutive equation derived by Henry Darcy based on experiments in hydrology and steady-state flow through a uniform porous medium in a single direction [20]. The law is a proportionality relationship between gradient of the applied pressure p and the fluid velocity through the medium $\boldsymbol{u}$,

$$\boldsymbol{u} = -\frac{K}{\mu}\nabla p, \tag{3.1}$$

where μ is the fluid viscosity (assumed constant) and K is the permeability. In this chapter, properties of incompressible fluid flow are examined, where the incompressibility condition is

$$\nabla \cdot \boldsymbol{u} = \frac{1}{r}\frac{\partial\left(ru_r\right)}{\partial r} + \frac{1}{r}\frac{\partial u_\theta}{\partial \theta} = 0, \tag{3.2}$$

where $\nabla\cdot$ is the divergence operator in cylindrical coordinates, and the velocity vector $\boldsymbol{u} = (u_r, u_\theta)$ for the radial velocity u_r and the angular velocity u_θ. In this thesis, a two-dimensional flow of air through a porous circular cylinder with radius R is examined, so using a tilde to denote dimensionless values, the variables

$$\boldsymbol{u} = \tilde{\boldsymbol{u}}U, \quad r = \tilde{r}R, \quad K = \tilde{K}K_{\text{Ref}}, \quad \nabla = \frac{\tilde{\nabla}}{R}, \quad \nabla^2 = \frac{\tilde{\nabla}^2}{R^2},$$

are defined, where U, R and K_{Ref} are characteristic scales for velocity, length, and permeability, respectively. A nondimensional variable for pressure, P, is introduced as

$$P = \frac{p - p_\infty}{\frac{1}{2}\rho U^2}, \tag{3.3}$$

where p_∞ is constant reference pressure far from the porous object and ρ is the density of the fluid, which is assumed constant in this chapter. This nondimensionalization is known as the pressure coefficient and is often used in fluid dynamics [15]. It represents the nondimensional difference relative to a given reference pressure. The nondimensional form of Darcy's law can be expressed as

$$\tilde{\boldsymbol{u}} = -c\tilde{K}\tilde{\nabla}P, \tag{3.4}$$

where

$$c = \frac{\frac{1}{2}\rho U K_{\text{Ref}}}{\mu L}. \tag{3.5}$$

Applying the incompressibility condition in its dimensionless form

$$\tilde{\nabla} \cdot \tilde{\boldsymbol{u}} = 0, \tag{3.6}$$

to Darcy's law yields

$$0 = \tilde{\nabla} \cdot \left(\tilde{K} \tilde{\nabla} P \right) = \tilde{\nabla} \tilde{K} \cdot \tilde{\nabla} P + \tilde{K} \cdot \tilde{\nabla}^2 P. \tag{3.7}$$

The boundary conditions for this problem are given by either the Dirichlet conditions for which P is specified, or the Neumann conditions $\nabla P \cdot \hat{n}$ for which the flow across the boundary is specified (because of Darcy's law). In the case where $\tilde{K}$ is constant, (3.7) becomes

$$0 = \tilde{\nabla}^2 P = \frac{\partial^2 P}{\partial \tilde{r}^2} + \frac{1}{\tilde{r}} \frac{\partial P}{\partial \tilde{r}} + \frac{1}{\tilde{r}^2} \frac{\partial^2 P}{\partial \theta^2}. \tag{3.8}$$

Based on the maximal principle for linear elliptic equations, it is known that the solution to this equation will take its maximum on the boundary [23]. If $\tilde{K}$ is a function of $\tilde{r}$ only, the equation is the only moderately more complex

$$0 = \left(\frac{\partial \tilde{K}}{\partial \tilde{r}} + \frac{\tilde{K}}{\tilde{r}} \right) \frac{\partial P}{\partial \tilde{r}} + \tilde{K} \frac{\partial^2 P}{\partial \tilde{r}^2} + \frac{\tilde{K}}{\tilde{r}^2} \frac{\partial^2 P}{\partial \theta^2}. \tag{3.9}$$

This equation is an example of a Sturm-Liouville problem, however it is singular, not regular.

3.1.1 Constant Permeability Solution

A classical problem for steady-state flow around an obstacle is to assume a one-dimensional flow far from the obstacle, with constant velocity moving parallel to the x-axis, where x and y are the horizontal and vertical components, respectively, in the standard Cartesian coordinate system. In this case, it is reasonable to assume that for an obstacle that is symmetric across the x-axis, such as a cylinder, the flow properties will be symmetric across the x-axis, as well. Mathematically, in Cartesian coordinates, the flow far from the obstacle as $x \to \pm\infty$ is defined as $\boldsymbol{u} = (-U, 0)$, that is, moving with constant speed U in the negative x-direction. This implies that boundary conditions that are even in terms of θ can be applied to the surface of the cylinder. With enough terms, any set of even boundary conditions can be reasonably approximated by a cosine series,

$$P(1, \theta) = \sum_{n=0}^{N} a_n \cos(n\theta). \tag{3.10}$$

While we will mostly consider a cosine series representing a fit to experimental data of turbulent flow over a cylinder, for comparison purposes the solution to the simplest flow past a circular cylinder will be considered. This simplest situation is the well-known case of inviscid flow, with no circulation about a cylinder. It should be noted that this is a purely theoretical flow that is not physically realizable. As given by [15], the pressure in the case of inviscid, irrotational flow described above about a solid cylinder is given exactly by

$$P(1,\theta) = 1 - 4\sin^2(\theta) = 2\cos(2\theta) - 1. \tag{3.11}$$

By applying separation of variables to equation (3.8), it can be shown that for the cosine series boundary conditions, the pressure through a porous cylinder with constant permeability is given by

$$P(\tilde{r},\theta) = \sum_{n=0}^{N} a_n \tilde{r}^n \cos(n\theta). \tag{3.12}$$

Setting the pressure about a solid cylinder for an inviscid flow as the boundary conditions for flow through a porous cylinder, this implies that the pressure in the cylinder's interior is

$$P(\tilde{r},\theta) = 2\tilde{r}^2\cos(2\theta) - 1. \tag{3.13}$$

Taking the dimensionless form of Darcy's law,

$$\tilde{\boldsymbol{u}} = -c\tilde{K}\tilde{\nabla}P, \tag{3.14}$$

and setting $c\tilde{K} = 1$, this implies that the velocity vector inside the cylinder is given by

$$\tilde{\boldsymbol{u}} = (\tilde{u}_{\tilde{r}}, \tilde{u}_\theta) = (-4\tilde{r}\cos(2\theta), 4\tilde{r}\sin(2\theta)), \tag{3.15}$$

where $\tilde{u}_{\tilde{r}}$ and $\tilde{u}_\theta$ are the dimensionless radial and angular components of velocity, respectively. Figure 3.2 compares this analytical solution to the numerical solution obtained with spectral code, which shows very good agreement. The maximum relative error in the numerical solution is 1.35×10^{-10}, indicating that the spectral method used in this problem yields satisfying results that approach machine precision. Since the solution in this case contains only a single mode, however, it is possible that higher mode solutions, such as for the turbulent flow boundary conditions described below, may yield higher relative errors. As a note, in the pressure profiles in this thesis, the colouration represents different pressure levels as indicated by the colour bars, and the vectors indicate relative fluid velocity.

The pressure about a solid cylinder for a constant velocity fluid flow where the Reynolds number $\mathrm{Re} = 7 \times 10^5$ is presented in Figure 3.1. The nearly constant region from roughly

135° to 180° indicates the region of the turbulent wake. Since this pressure data was unavailable, it was approximated using a function constructed on the domain 0 to π that includes the important features of the data,

$$P(1,\theta) = 1.0488\left(\frac{1}{2} - \frac{\arctan(8\theta - 16)}{\pi}\right)\left(1 - 3.5\, e^{-2\left(\theta - \frac{\pi}{2}\right)^2}\right) \tag{3.16}$$

$$- 0.10488\left(\frac{1}{2} + \frac{\arctan(8\theta - 16)}{\pi}\right)\left(1 + 22\, e^{-14\left(\theta - \frac{197}{100}\right)^2}\right). \tag{3.17}$$

The even extension of this function was determined to obtain boundary conditions that were symmetric across the x-axis, and was approximated using the first fifteen terms of a cosine series. The numerically determined pressure profile and velocity field are presented in Figure 3.3.

The key feature of the constant permeability inviscid case is the symmetry of the flow. Since the boundary conditions (3.11) are symmetric across the x- and y-axes, the flow through the cylinder is symmetric across both of the axes, as well. Since the turbulent flow boundary conditions are even across the x-axis only, the resulting flow through the disc is symmetric across the x-axis only. The flows through both distributions exhibit the same behaviour, as the fluid moves from the regions of high pressure near $\theta = 0$ and $\theta = \pi$ to the regions of low pressure near $\theta = \pi/2$ and $\theta = 3\pi/2$. In the turbulent case, however, the flow through the left half of the cylinder is less significant than the flow through the right half, since the left half of the cylinder is comprised mostly of the low pressure turbulent region, resulting in a smaller pressure gradient. Figure 3.4 plots the radial velocities through the boundaries for both cases. The velocity plot for the turbulent BCs takes the same overall shape as the plot for the inviscid BCs, but with several small scale features. The turbulent BCs also result in greater maximum radial velocities near $\theta = \pi/2$ and $\theta = 3\pi/2$, suggesting greater pressure gradients in those regions for the turbulent BCs.

3.2 Modeling Different Permeabilities

Code was developed in Matlab to solve the porous media Laplace equation for pressure for a given permeability distribution and set of boundary conditions on a disc, using the transformation into Fourier space for the azimuthal variable. The code uses a radial domain of $-1 \leq \tilde{r} \leq 1$ and an angular domain of $0 \leq \theta \leq 2\pi$, so each point in the disc is covered twice. The change of the angular variables into wave numbers allows for an efficient separation of variables, in that it solves an ODE in terms of the radial coordinate on a

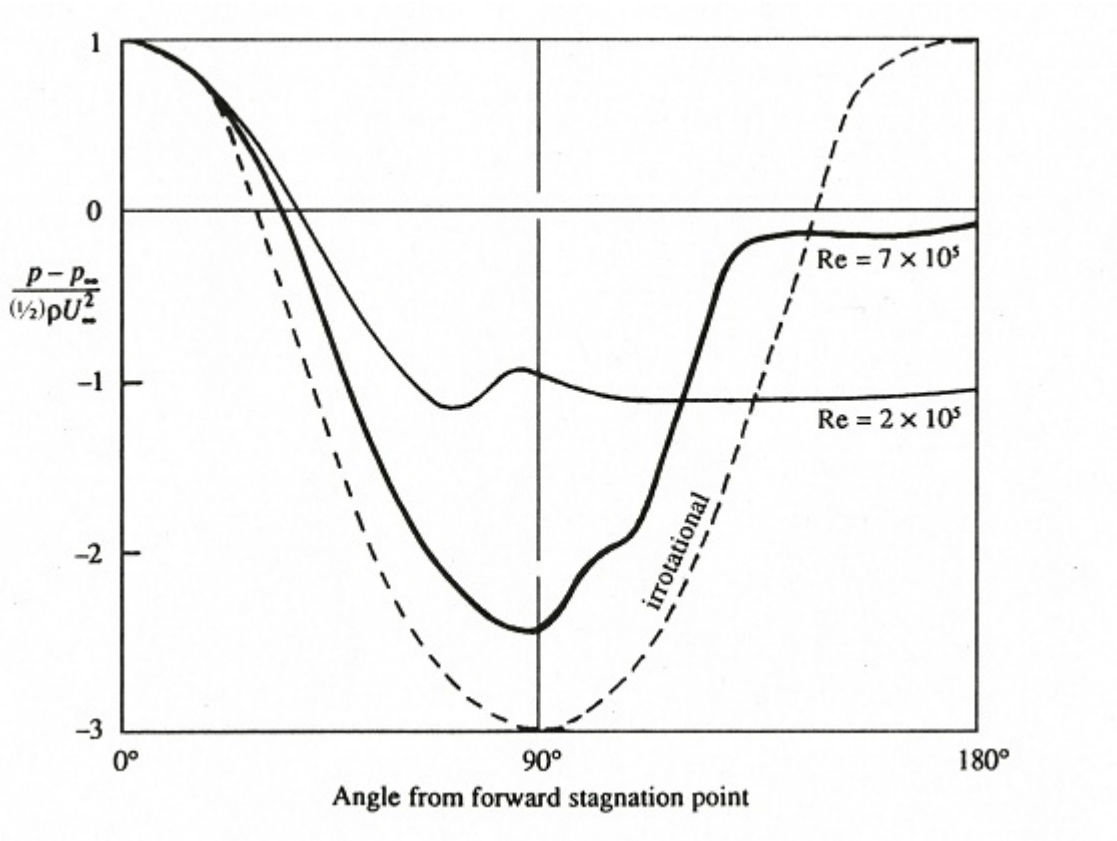

Figure 3.1: Dimensionless pressure distributions with respect to the forward stagnation point for fluid flow about a solid cylinder. The dotted line represents the analytical distribution for an inviscid, irrotational flow, while the solid lines indicate distributions for subcritical ($\mathrm{Re} = 2 \times 10^5$) and supercritical ($\mathrm{Re} = 7 \times 10^5$) Reynolds number flows [15]. At the critical Reynolds number, $\mathrm{Re}_{Cr} \sim 3 \times 10^5$, the laminar boundary develops instabilities and transitions into a turbulent boundary layer. The near constant regions in the subcritical and supercritical distributions indicate turbulent wakes.

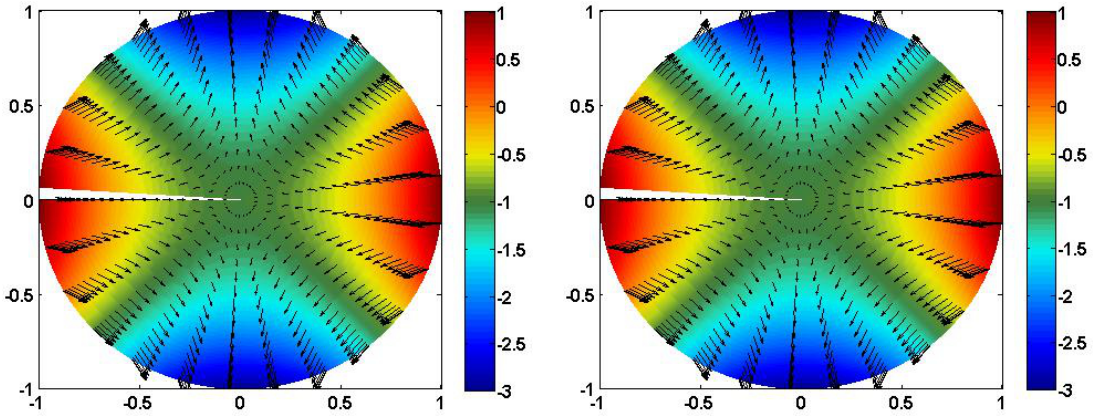

(a) (b)

Figure 3.2: Pressure distributions of the exact (a) and numerical (b) solutions for inviscid flow through a porous cylinder with constant permeability.

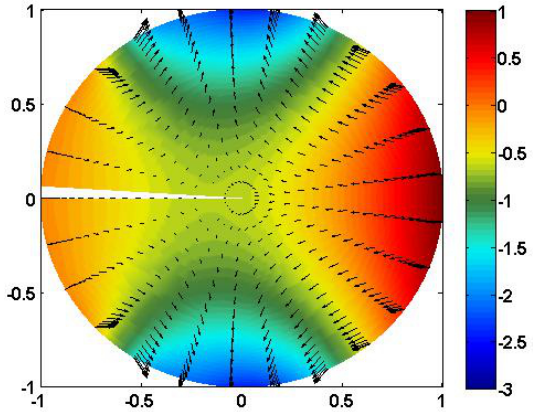

Figure 3.3: Pressure profile and velocity field through a porous cylinder with constant permeability and turbulent boundary conditions.

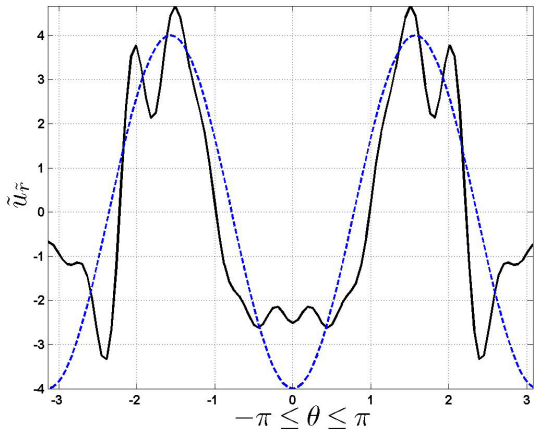

Figure 3.4: Radial velocity through the boundary of a constant permeability cylinder for the turbulent BCs (solid line) and the inviscid BCs (dashed line).

Chebyshev grid for each value of the Fourier variable. In particular, this conversion of the 2D problem to several tens of 1D problems allowed the use of 402 Chebyshev grid points in the radial direction. This grid size is somewhat larger than what a typical Chebyshev method would use. 100 grid points were used in the angular direction.

Several permeability distributions as functions of $\tilde{r}$ were designed to simulate different porous medium distributions. In order to accommodate the trick of using the $-1 \leq \tilde{r} \leq 1$ radial domain, the permeability equations must be even in $\tilde{r}$. Special care also needs to be taken to use enough grid points in the radial direction to sufficiently resolve the different features of the permeabilities (this explains the large number of grid points in the radial direction). It should be noted that the length of the velocity vectors is determined relative to the smallest velocity in a given plot, so velocity magnitudes cannot be directly compared between different pressure profiles.

3.2.1 Slowly decreasing permeability

The first distribution,

$$\tilde{K}(\tilde{r}) = \frac{1}{1+c}\left(\cos\left(\pi\tilde{r}\right) + c\right), \tag{3.18}$$

represents a permeability that slowly decreases moving from the centre of the cylinder (the pile) out to its exterior. The constant coefficient guarantees that the maximum permeability at the centre will be 1, while the choice of c determines the minimum permeability.

Figure 3.5 presents the pressure profiles, velocity fields, and scaled radial velocities normal to the surface of the cylinder for the cases in which $c = 5/3$, $c = 3$ and $c = 7$. The values of c represent minimum permeabilities of $\tilde{K} = 0.25$, $\tilde{K} = 0.5$, and $\tilde{K} = 0.75$ at the edge of the cylinder, respectively. In these simulations, and the remaining simulations for flow through a cylinder in this chapter, the turbulent boundary conditions were used.

There are very few, if any, noticeable differences in each of these simulations. As the value of c increases, and thus the permeability near the boundary increases, the velocity of the fluid near the centre of the cylinder appears to decrease relative to the velocity throughout the rest of the cylinder. This makes sense, as the lower minimum boundary permeability cases would be expected to have lower velocities further from the centre of the cylinder. The velocity in the centre will therefore be higher relative to these velocities. There also appears to be slightly more yellow colouration in the centre as c increases, implying higher pressure and thus deeper penetration by the fluid. This also makes sense, as the more permeable cylinders should allow greater fluid flow.

3.2.2 Slowly increasing permeability

The second distribution,

$$\tilde{K}(\tilde{r}) = \frac{1}{1+c}\left(c - \cos\left(\pi\tilde{r}\right)\right), \tag{3.19}$$

represents a permeability that slowly increases moving from the centre of the pile to its exterior. As before, the constant coefficient guarantees that the maximum permeability will be 1, while the choice of c determines the minimum permeability. Figure 3.6 presents the cases in which $c = 5/3$, $c = 3$ and $c = 7$, which represent minimum permeabilities of $\tilde{K} = 0.25$, $\tilde{K} = 0.5$, and $\tilde{K} = 0.75$, respectively. As with the previous permeability case, differences between each simulation are difficult to discern. As the value of c increases, and thus the permeability near the centre increases, there appears to be a very minor relative increase in velocity near the centre. Although it is difficult to notice, at also appears that the pressure near the centre appears to be greater for larger values of c, which can be explained as these distributions having greater average permeabilities as c increases.

The slowly decreasing and slowly increasing permeability cases show very similar behaviour. As in the constant permeability case, the direction of flow is from the high pressure regions in the left and right parts of the cylinder to the low pressure regions at the top and bottom. Since the pressure is much higher near the right hand side than near the left hand side, the relative flow is greater there. In both the increasing and decreasing permeability cases, higher values of c result in higher average permeabilities, and thus deeper fluid penetration and higher pressures near the centre.

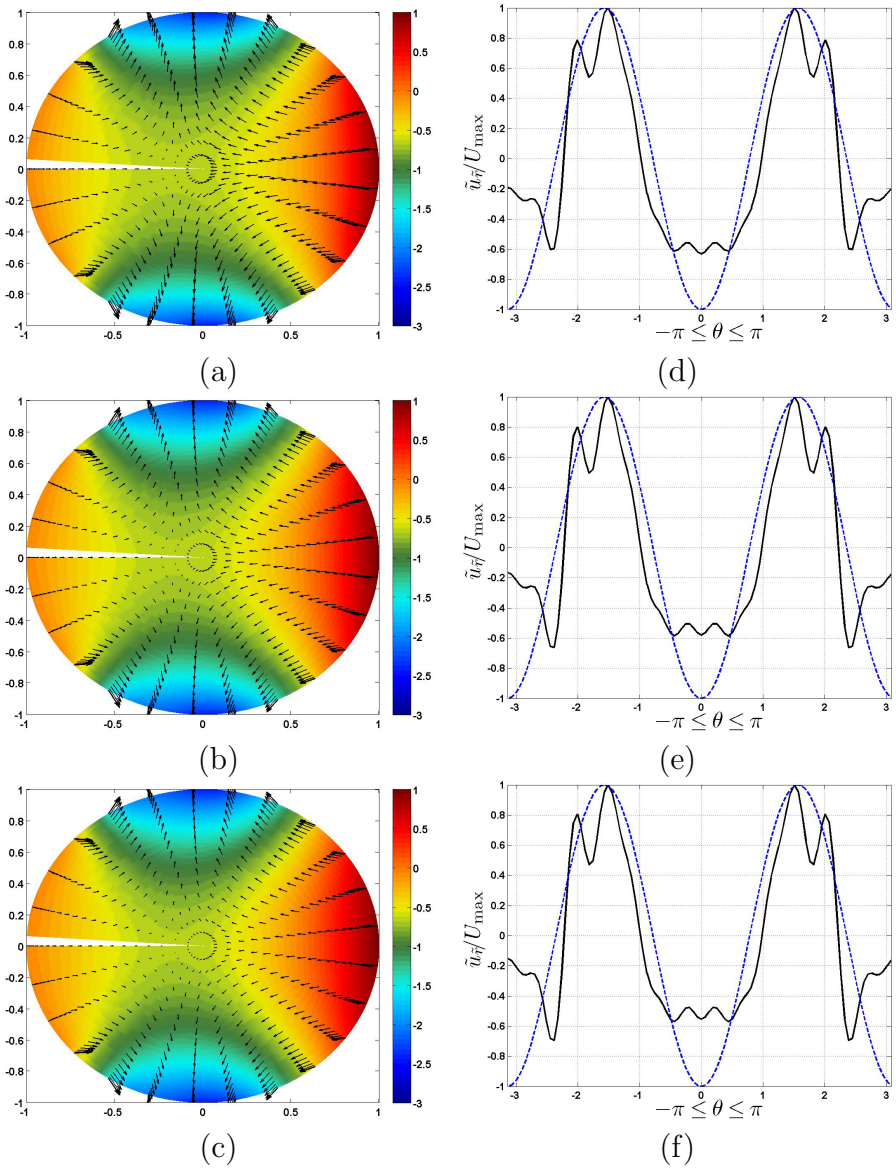

Figure 3.5: Pressure and velocity fields of fluid flow through a permeable disc ((a)-(c)), where the permeability is defined by equation (3.18), and the scaled radial velocity normal to the surface of the cylinder, $\tilde{u}_{\tilde{r}}/U_{\max}$, where $U_{\max} = \max|\tilde{u}_{\tilde{r}}|$, as a function of θ ((d)-(f)). The solid line is the case of turbulent flow about a cylinder with permeability defined by (3.18), while the dotted line is the inviscid flow about a cylinder of constant permeability. For each plot, the values of c are (a),(d), $c = 5/3$; (b),(e) $c = 3$; (c),(f), $c = 7$.

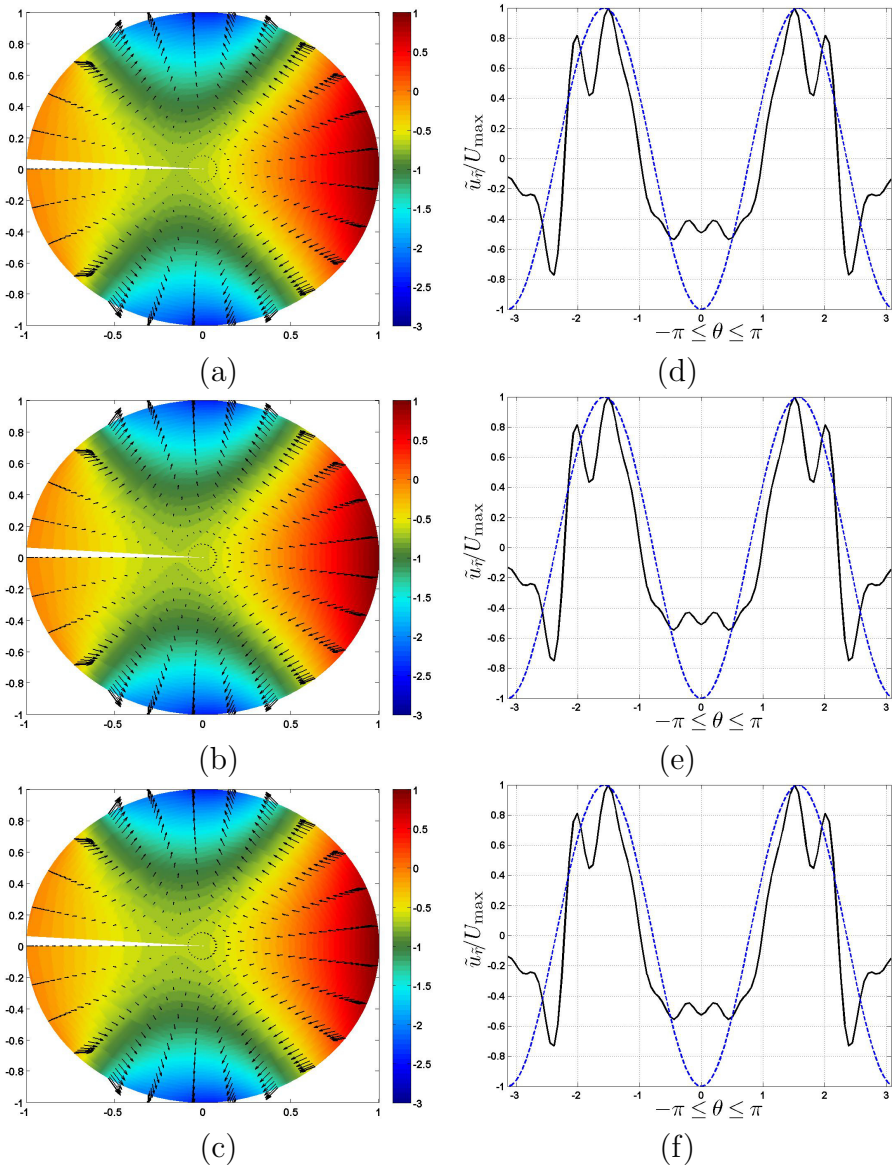

Figure 3.6: Pressure and velocity fields of fluid flow through a permeable disc ((a)-(c)), where the permeability is defined by equation (3.19), and the scaled radial velocity normal to the surface of the cylinder, $\tilde{u}_{\tilde{r}}/U_{\max}$, where $U_{\max} = \max|\tilde{u}_{\tilde{r}}|$, as a function of θ ((d)-(f)). The solid line is the case of turbulent flow about a cylinder with permeability defined by (3.19), while the dotted line is the inviscid flow about a cylinder of constant permeability. For each plot, the values of c are (a),(d), $c = 5/3$; (b),(e) $c = 3$; and (c),(f), $c = 7$.

3.2.3 Near constant permeability with a narrow hole

The third distribution,

$$\tilde{K}(\tilde{r}) = d\left(e^{-b(\tilde{r}-a)^2} + e^{-b(\tilde{r}+a)^2} + c\right), \tag{3.20}$$

where

$$d = \frac{1}{e^{-4ba^2} + c + 1}, \tag{3.21}$$

simulates a densely packed material of low permeability with a narrow region of significantly higher permeability (due to larger rocks, for example), which is labeled somewhat loosely as a hole. In this equation, a is a constant that determines the location of the centre of the hole, b is a constant that defines the width of the hole, c is a small positive constant that ensures the permeability is large enough to permit noticeable flow (i.e., ensures nonzero permeability), and d is a constant that normalizes the maximum of the permeability to 1. Setting $c = 0.01$, several experiments were performed using various values of a and b, as shown in Figure 3.7. In each case, the high permeability region of the disc has the highest relative rate of flow, with fluid moving from the high pressure boundary region to the low pressure boundary region, traveling mostly through the annulus defined by the hole. These regions of high flow are wider in the $b = 100$ cases, which is to be expected, as the high permeability peaks occupy a larger portion of the domain in these cases. At the interior of the annulus of high flow where the permeability is near zero and near constant, there appears to be a region of zero flow. Physically this can be explained as the fluid taking the path of least resistance along the hole to reach the low pressure boundary. This suggests that flow can be guided along high permeability channels or voids, and that this may be a useful method to force flow in a particular direction. The problem is, however, that in the simulations in Figure 3.7, the minimum permeability is about 1% of the maximum permeability, so determining the difference between minimum and maximum permeability resulting in noticeable guided flow is important. Most of the domain in these simulations is near impermeable, anyway, which implies that very minimal flow is observed. As the hole was moved closer to the exterior of the disc, the fluid velocity at the boundary appeared to increase. Also in each case, the fluid appeared to move fastest along the hole, with the fluid velocity decreasing from the centre of the hole into the disc's interior where it was near zero. It appeared that the region of near zero velocity was between the centre of the cylinder and the beginning of the hole. This makes sense as it will be easier for the fluid to move through the region with the most open space, so more fluid will move through the high permeability region, leaving less to flow through the low permeability interior of the disc, reducing the fluid velocity (via conservation of mass). The scaled velocity profiles in

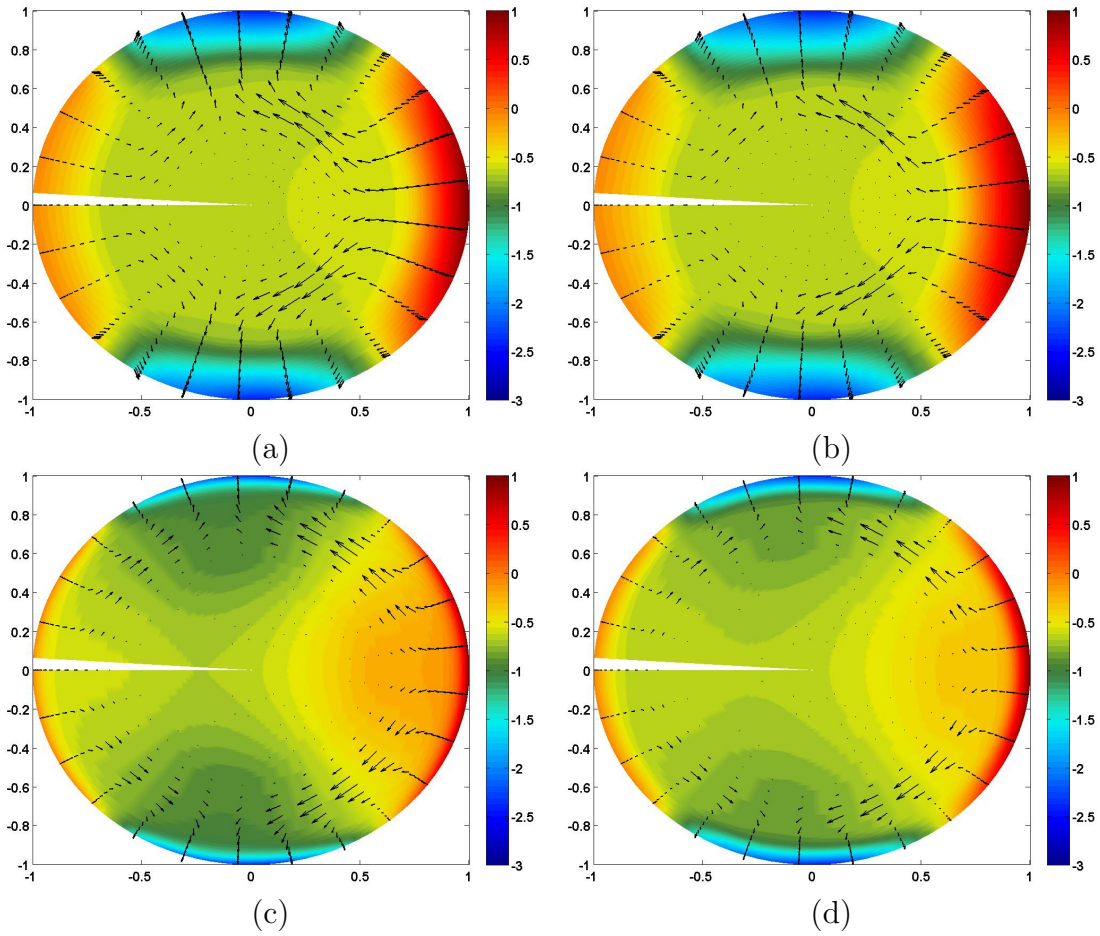

Figure 3.7: Pressure and velocity fields of fluid flow through a permeable disc, where the permeability is defined by equation (3.20). In each case, $c = 0.01$, and the remaining constants are (a) $a = 0.5$, $b = 100$; (b) $a = 0.5$, $b = 200$; (c) $a = 0.75$, $b = 100$; (d) $a = 0.75$, $b = 200$.

Figure 3.9 all possess the same general shape, but in the cases where $a = 0.75$, the small scale features are smoothed out considerably.

3.2.4 Near constant permeability with a narrow blockage

The fourth distribution,

$$\tilde{K}(\tilde{r}) = c - d\left(e^{-b(\tilde{r}-a)^2} + e^{-b(\tilde{r}+a)^2}\right), \tag{3.22}$$

represents the opposite case to the first, where the permeability is constant and relatively high throughout most of the domain, with a negative Gaussian distribution providing a steep and symmetric decrease to much lower permeability to simulate a low permeability blockage in the porous material (a region in which fine grained material is mixed into the pile). In this equation, a, b, c and d are constants defining the centre of the blockage, the width of the blockage, the constant high permeability throughout most of the domain, and the minimum value of the permeability, respectively. Setting $c = 1$ and $d = 0.99$, experiments were performed by varying the value of a and b, shown in Figure 3.10. In each case the flow tends to follow a path along the annular region for $a < \tilde{r} < 1$ from the high pressure boundary to the low pressure boundary. Almost every pressure distribution also shows a region of near zero flow for $\tilde{r} < a$. There is an exception, however, in the $a = 0.5$, $b = 500$ case in the $\tilde{r} < a$ region, where there is flow from the higher pressure areas near $\theta = 0$ and $\theta = \pi$ in toward the centre of the disc, and flow leaving the centre of the cylinder toward the low pressure regions near $\theta = \pi/2$ and $\theta = 3\pi/2$. In the scaled velocity profiles in Figure 3.12, the small scale features are more pronounced in the $a = 0.75$ cases than in the $a = 0.5$ cases. Also, Figure 3.12 (c) is unique among the cylindrical simulations presented in this chapter, as it is the only case that has a largest radial velocity normal to the surface of the cylinder that is negative.

3.2.5 General Results

As expected based on Darcy's law, areas of low permeability experience relatively less flow than areas of high permeability. The simulations involving narrow regions of high permeability in a nearly impermeable cylinder indicate that high permeability paths through piles may be able to direct flow along a desired route. One would need to ensure that the endpoint of such a path is near the low pressure boundary, as fluid may leach through the low permeability areas of the pile if the low pressure boundary is elsewhere. This is shown

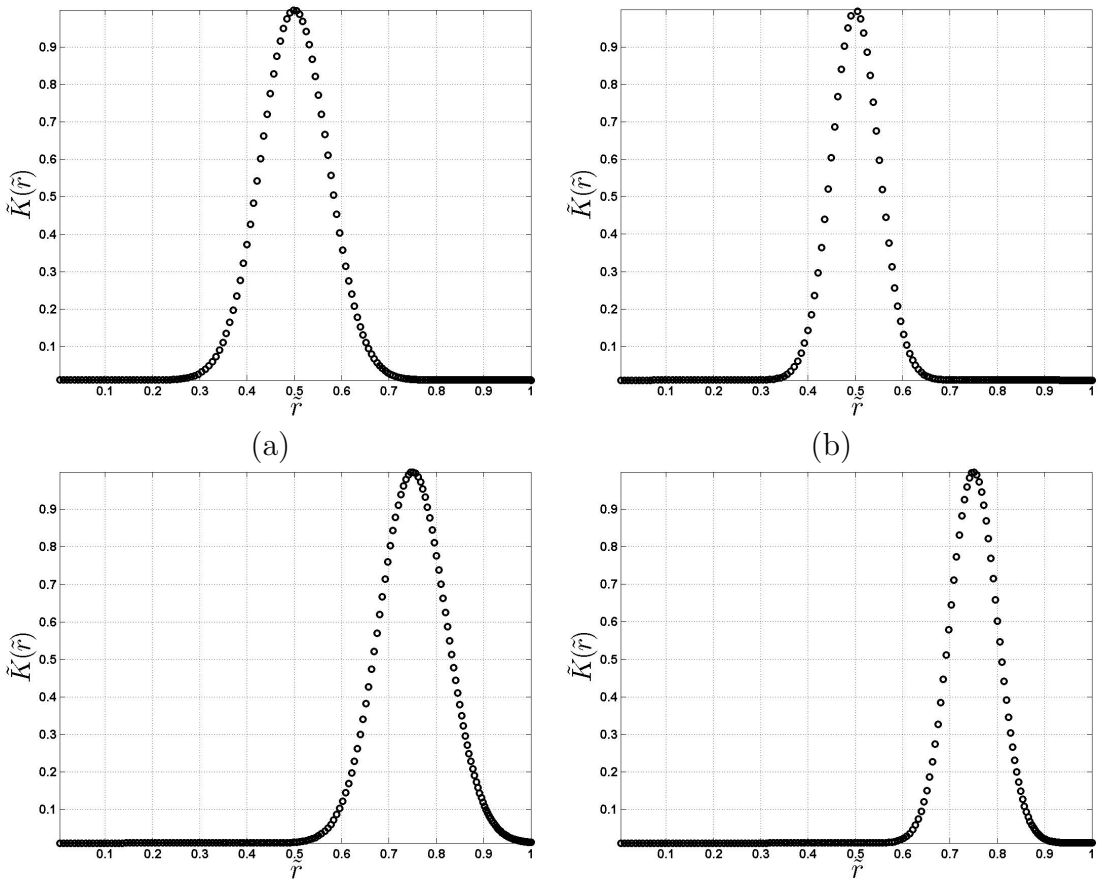

Figure 3.8: Permeability profiles as a function of $\tilde{r}$ as defined by equation (3.20). In each case, $c = 0.01$, and the remaining constants are (a) $a = 0.5$, $b = 100$; (b) $a = 0.5$, $b = 200$; (c) $a = 0.75$, $b = 100$; (d) $a = 0.75$, $b = 200$.

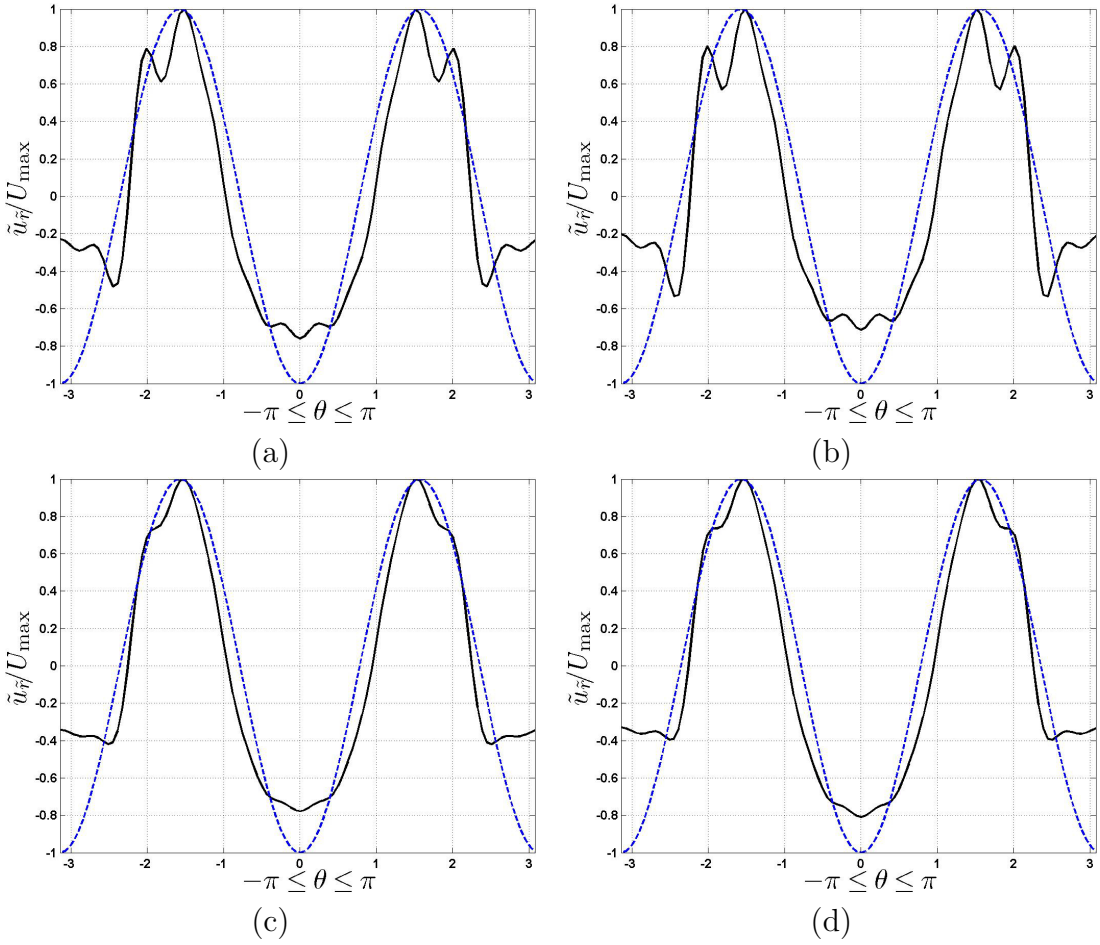

Figure 3.9: The scaled radial velocity normal to the surface of the cylinder, $\tilde{u}_{\tilde{r}}/U_{\max}$, where $U_{\max} = \max|\tilde{u}_{\tilde{r}}|$, as a function of θ. The solid line is the case of turbulent flow about a cylinder with permeability defined by equation (3.20), while the dotted line is the inviscid flow about a cylinder of constant permeability. In each case, $c = 0.01$, and the remaining constants are (a) $a = 0.5$, $b = 100$; (b) $a = 0.5$, $b = 200$; (c) $a = 0.75$, $b = 100$; (d) $a = 0.75$, $b = 200$.

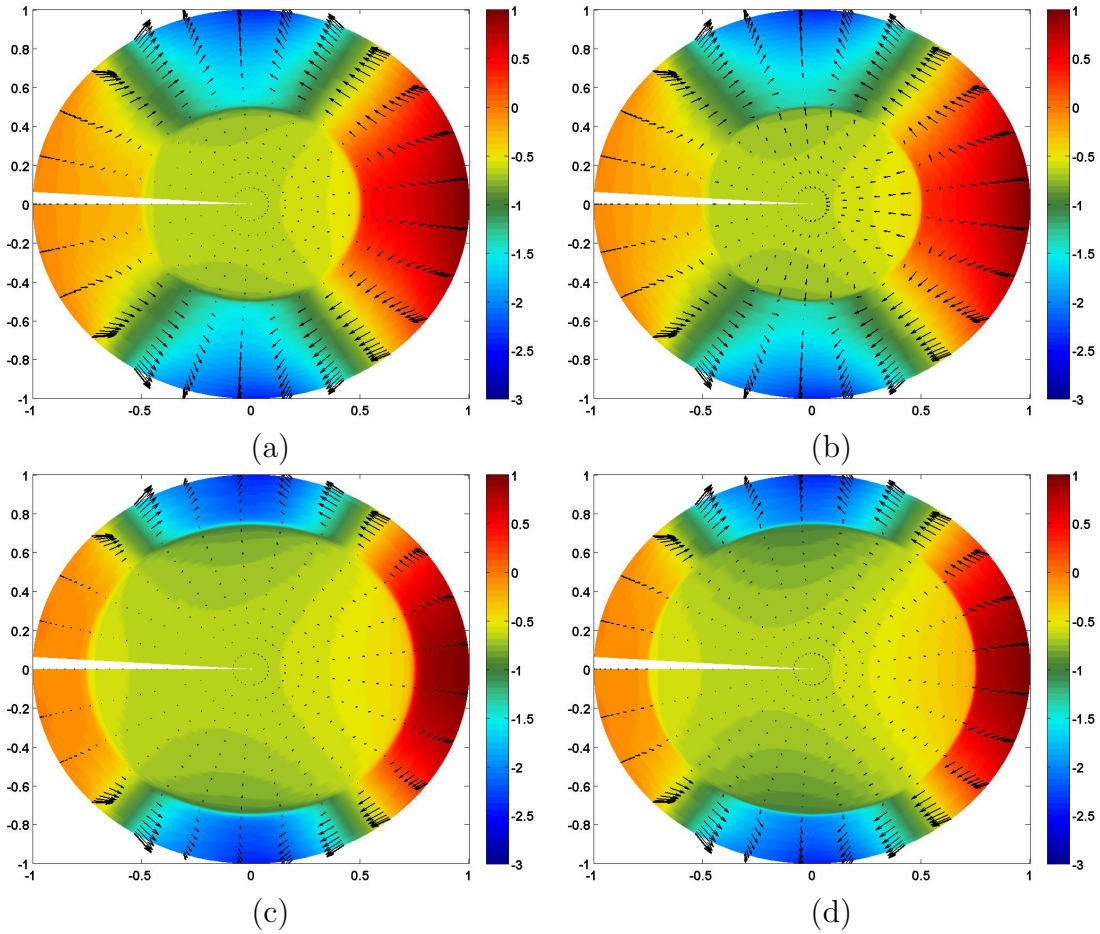

Figure 3.10: Pressure and velocity fields of fluid flow through a permeable disc, where the permeability is defined by equation (3.22). In each case, $c = 1$, $d = 0.99$, and the remaining constants are (a) $a = 0.5$, $b = 100$; (b) $a = 0.5$, $b = 500$; (c) $a = 0.75$, $b = 100$; (d) $a = 0.75$, $b = 500$.

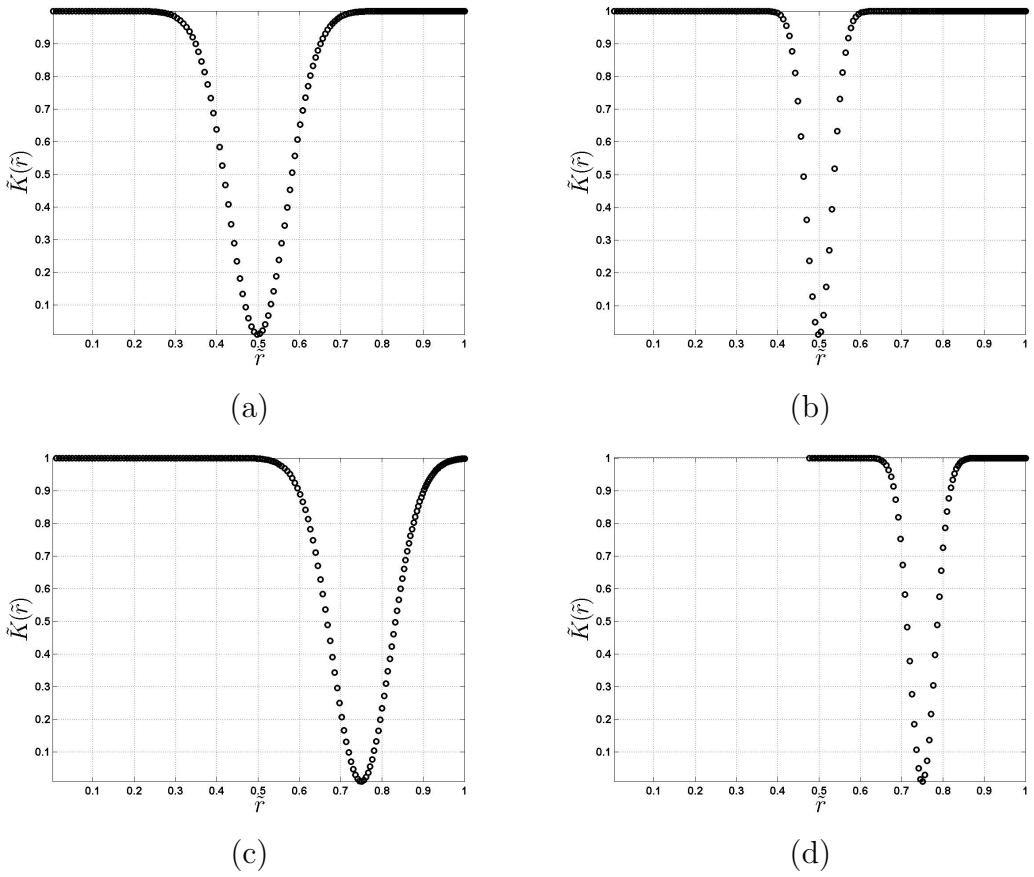

Figure 3.11: Permeability profiles as a function of $\tilde{r}$ as defined by equation (3.22). In each case, $c = 1$, $d = 0.99$, and the remaining constants are (a) $a = 0.5$, $b = 100$; (b) $a = 0.5$, $b = 500$; (c) $a = 0.75$, $b = 100$; (d) $a = 0.75$, $b = 500$.

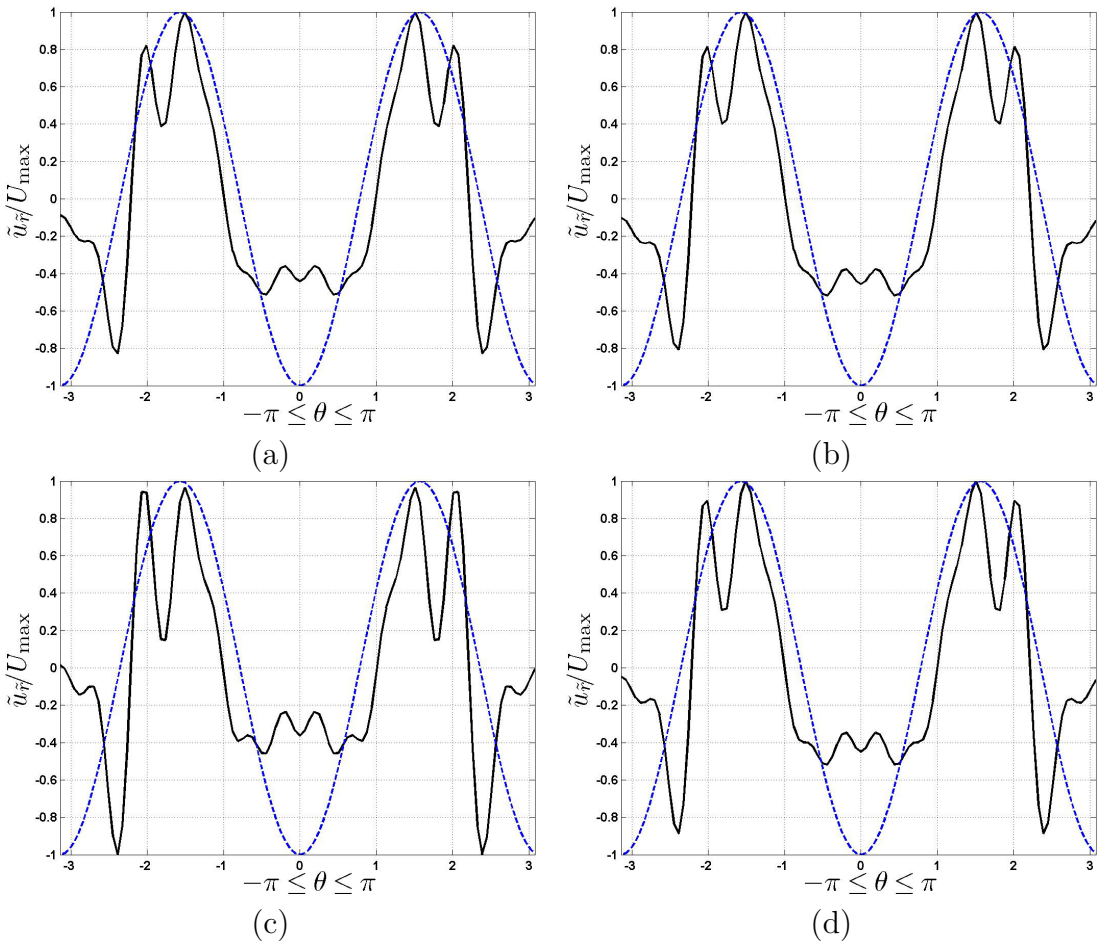

Figure 3.12: The scaled velocity normal to the surface of the cylinder, $\tilde{u}_{\tilde{r}}/U_{\max}$, where $U_{\max} = \max|\tilde{u}_{\tilde{r}}|$, as a function of θ. The solid line is the case of turbulent flow about a cylinder with permeability defined by equation (3.22), while the dotted line is the inviscid flow about a cylinder of constant permeability. In each case, $c = 1$, $d = 0.99$, and the remaining constants are (a) $a = 0.5$, $b = 100$; (b) $a = 0.5$, $b = 500$; (c) $a = 0.75$, $b = 100$; (d) $a = 0.75$, $b = 500$.

in Figure 3.7, where near $\theta = \pi/2$ and $\theta = 3\pi/2$ the fluid travels from the high permeability hole out to the low pressure boundary. The simulations involving narrow regions of low permeability show that even a thin layer of low permeability material can effectively prevent flow inside the pile. This suggests that this may be an acceptable method for controlling flow. This could be achieved by adding a layer of finely crushed material only along the region where fluid flow needs to be prevented, and not over the entire pile. Although these results were obtained using high order numerical methods and provide some interesting conceptual information, it would be beneficial to observe the effect of these permeability distributions on flow in a domain more representative of an actual waste rock pile. This can be achieved through the use of finite element methods.

3.3 Modeling with Finite Element Methods

While the accuracy of the previously discussed spectral methods is very high, they cannot model a domain that reflects an arbitrary pile shape. Note, however, that a trapezoidal pile could be handled via mapped coordinates. The use of mapped coordinates with spectral methods was briefly investigated, however they were determined to be too inefficient when trying to resolve the permeabilities of interest. As discussed in the Introduction, the three Diavik waste rock test piles are trapezoidal in shape, and are 15 m high with 20 m $\times$ 50 m upper surfaces, and angles of repose of approximately 37.5° for two of the piles, and 18.4° for the third pile. This type of geometry is easily handled by the finite element method, and indeed can be solved with many standard, off-the-shelf engineering packages since these often contain a CAD-like domain sketching environment. In the spirit of using models that are as transparent and rational as possible, the Matlab PDE toolbox [19] has been chosen to solve the steady state problem in the pile geometry.

The finite element method simulations are performed in Cartesian coordinates, so the the dimensionless pressure equation should be quickly recast in terms of these variables. The dimensionless horizontal and vertical position variables in Cartesian coordinates are defined as $\tilde{x} = x/L$ and $\tilde{y} = y/L$, respectively, where L is some characteristic length scale. The length scale is assumed to be the same in both directions as the height and width of the waste rock piles are on the same order of magnitude. In Cartesian coordinates, for a variable permeability $\tilde{K} = \tilde{K}(\tilde{x}, \tilde{y})$, equation (3.7) becomes

$$0 = \frac{\partial \tilde{K}}{\partial \tilde{x}} \frac{\partial P}{\partial \tilde{x}} + \frac{\partial \tilde{K}}{\partial \tilde{y}} \frac{\partial P}{\partial \tilde{y}} + \tilde{K} \left(\frac{\partial^2 P}{\partial \tilde{x}^2} + \frac{\partial^2 P}{\partial \tilde{y}^2} \right). \tag{3.23}$$

The domain was designed to represent a cross-section of the piles TI and TIII described in

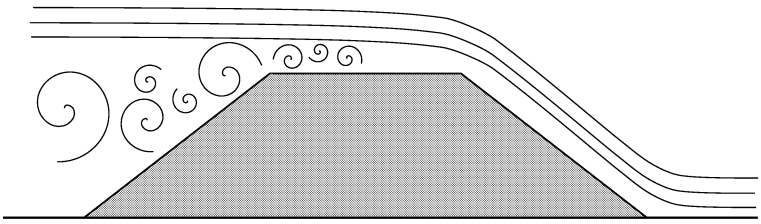

Figure 3.13: Hypothetical flow past a trapezoidal pile.

the introduction. The proportions are not identical, however, as the height of the domain is slightly too low. The problem is defined in the same way as the flow about the cylinder, that far from the pile the fluid is moving with a constant speed in the negative x-direction, and that the Reynolds number is high enough so that turbulence develops around the pile. Unfortunately, pressure distributions about a trapezoidal obstacle are not as widely studied, and hence they are not as readily available as pressure distributions about circular cylinders, so some estimation and modeling had to be carried out. The boundary conditions were designed to be similar to the conditions around a cylinder described above. A sketch of the hypothetical streamlines and turbulent region for flow past a trapezoidal pile is presented in Figure 3.13. As in the cylindrical case, pressure is assumed to decrease as one moves up the obstacle. In the turbulent region, pressure is assumed constant. Along the right face of the pile (which occupies the line $\tilde{y} = -\frac{13}{10}\tilde{x} + \frac{26}{5}$), pressure is assumed to linearly decay from 1 at the base of the pile down to 0 at the upper right corner of the pile. Thus along this face, pressure is equal to $1 - \frac{10}{13}\tilde{y}$. Along the surface at $\tilde{y} = 1.3$, the BCs were assumed to be $P(\tilde{x}, 1.3) = \frac{1}{4}\left(e^{4(\tilde{x}-3)} - 1\right)$, which is intended to simulate decay from a higher pressure of 0 down to a small negative constant pressure of $-1/4$ in the turbulent region part way across the upper surface of the pile. This is based on the idea that viscous flow across a flat plate will be laminar at first, but will undergo an instability and breakdown into turbulence as distance from the beginning of the plate increases [15]. The left face of the pile (which occupies the line $\tilde{y} = \frac{13}{10}\tilde{x}$) is assumed to reside completely within the turbulent region, so P is set equal to $-1/4$. Since the base of the pile is in contact with the ground, which is assumed to be solid, the flux through the base should be zero, and thus the boundary conditions along $\tilde{x} = 0$ are $\tilde{\nabla}P = 0$. Eight different permeabilities similar to those described for flow through a cylinder were used in examining flow through the pile. There is an added benefit to using the FEM since the permeability functions need not be even as in the spectral code. These simulations are presented in Figures 3.14, 3.15, 3.16 and 3.17. In computing these solutions, linear test functions are used by Matlab's PDE toolbox.

Figure 3.14 presents a constant permeability case (a) where $\tilde{K} = 1$, and a nearly constant permeability case with a narrow blockage running vertically through the centre of the pile (b). The latter is defined by the equation

$$\tilde{K}(\tilde{x}, \tilde{y}) = 1 - 0.9e^{-100(\tilde{x}-2)^2}. \tag{3.24}$$

In both cases the fluid enters through the right face of the pile and appears to exit mostly through the right half of the top face of the pile. The constant permeability case shows the fluid moving to the left and up, with the largest velocity vectors occurring near the bottom and top right corners. The higher vertically in the pile, the more the velocity vectors steepen and point upwards. For $\tilde{x} < 2$ the vectors are significantly smaller, and the pressure gradient seems much less significant, as the pressure inside the pile seems very close to the small negative constant boundary pressure in the turbulent region. The case with the vertical blockage is very similar, except it appears that near $\tilde{x} = 2$ the pressure is higher and the velocity vectors are steeper than in the constant permeability case. There is also a noticeable line in the latter case at $\tilde{x} = 2$ where pressure goes from small and positive to near zero or even negative. It appears that the velocity along this line is very close to zero.

The permeabilities presented in Figure 3.15 are both linear functions of $\tilde{x}$. In (c), $\tilde{K}$ increases as $\tilde{x}$ increases, and is given by $\tilde{K}(\tilde{x}, \tilde{y}) = \frac{1}{4}\tilde{x}$. In (d), $\tilde{K}$ decreases as $\tilde{x}$ increases, and is given by $\tilde{K}(\tilde{x}, \tilde{y}) = 1 - \frac{1}{4}\tilde{x}$. In each case $\tilde{K}$ ranges from 0 to 1. The increasing permeability case shows noticeably deeper fluid penetration on the right hand side of the pile than the decreasing case, which is easily explained by the fact that the permeability is significantly higher there in (c) than in (d). While there appears to be a slight pressure gradient in the left half of (c), the velocity vectors there are all near zero, since the permeability is smaller there and the pressure near those boundaries is small and constant.

The permeabilities presented in Figure 3.16 are similar to those Figures 3.15 in that they are increasing and decreasing linear functions of $\tilde{y}$. $\tilde{K}$ is given by $\tilde{K}(\tilde{x}, \tilde{y}) = \frac{10}{13}\tilde{y}$ in (e) and $\tilde{K}(\tilde{x}, \tilde{y}) = 1 - \frac{10}{13}\tilde{y}$ in (f). As permeability increases with $\tilde{y}$ in (e), there is noticeably less fluid penetration than in (f), where permeability decreases with $\tilde{y}$. These are similar to the cases presented in (c) and (d), as (d) and (e) have lower permeabilities in the region near the high pressure boundary in the bottom right corner, while (c) and (f) have much higher permeabilities in that region. This suggests that flow through the pile can be prevented or reduced if low permeability material is used in construction near high pressure boundaries.

In Figure 3.17, case (g) presents the effects of a narrow horizontal region of low perme-

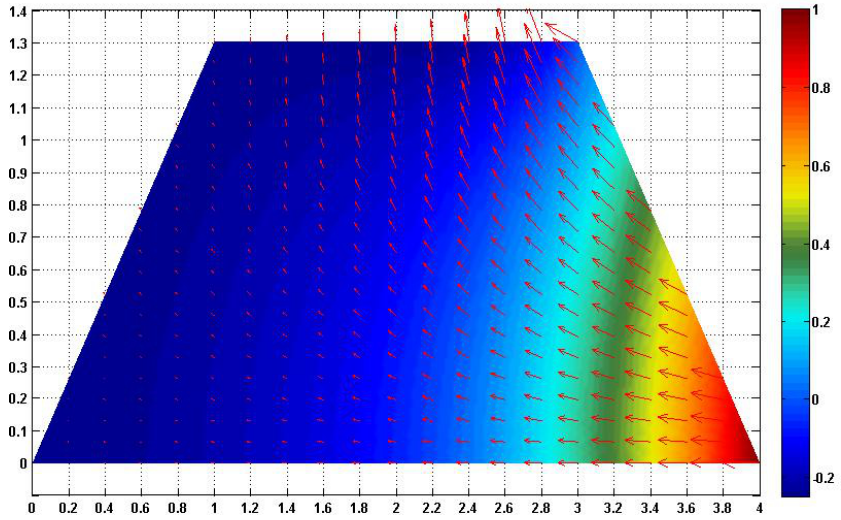

(a)

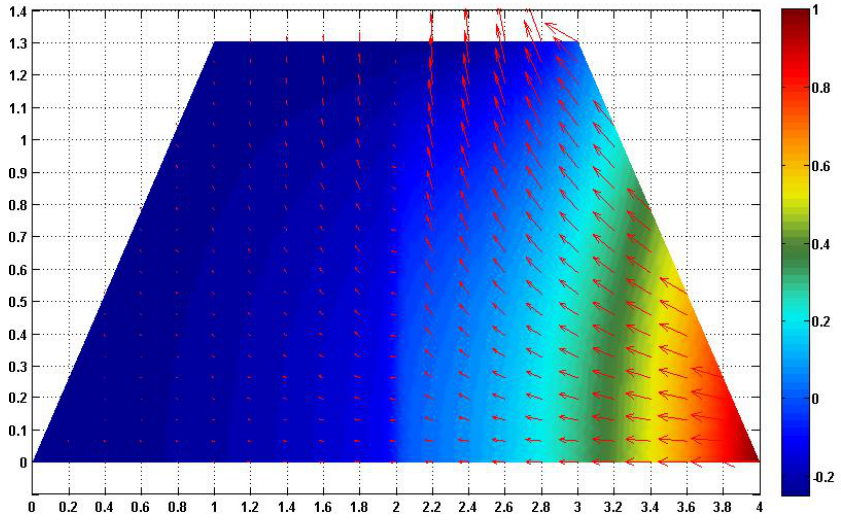

(b)

Figure 3.14: Pressure distributions for various permeabilities in a trapezoidal pile using a FEM. The permeabilities are given as (a) $\tilde{K} = 1$ and (b) $\tilde{K} = 1 - 0.9e^{-100(\tilde{x}-2)^2}$.

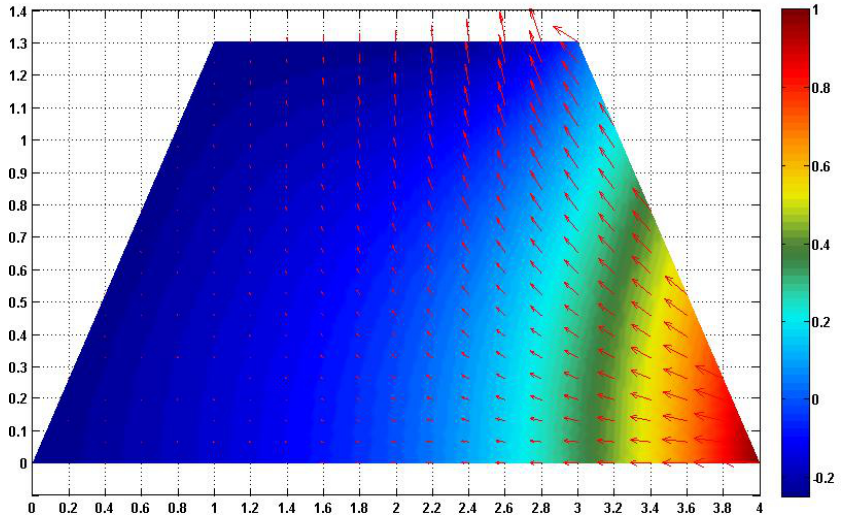

(c)

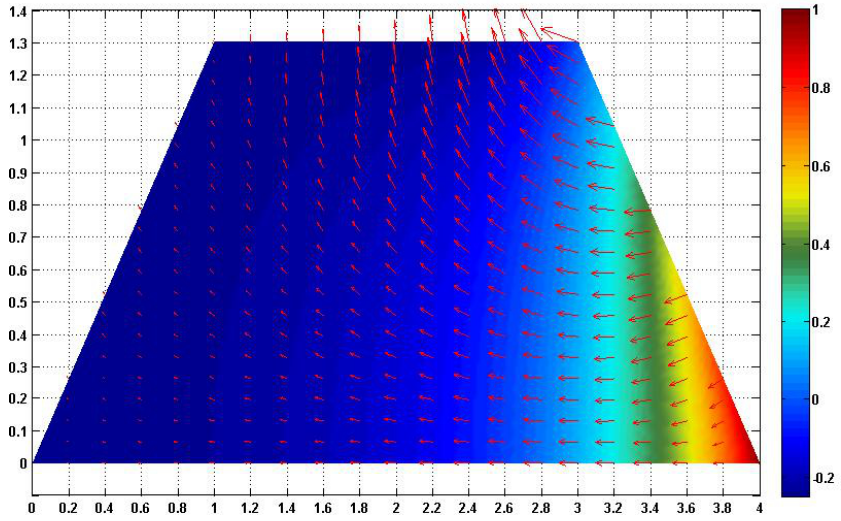

(d)

Figure 3.15: Pressure distributions for various permeabilities in a trapezoidal pile using a FEM. The permeabilities are given as (c) $\tilde{K} = \frac{1}{4}\tilde{x}$ and (d) $\tilde{K} = 1 - \frac{1}{4}\tilde{x}$.

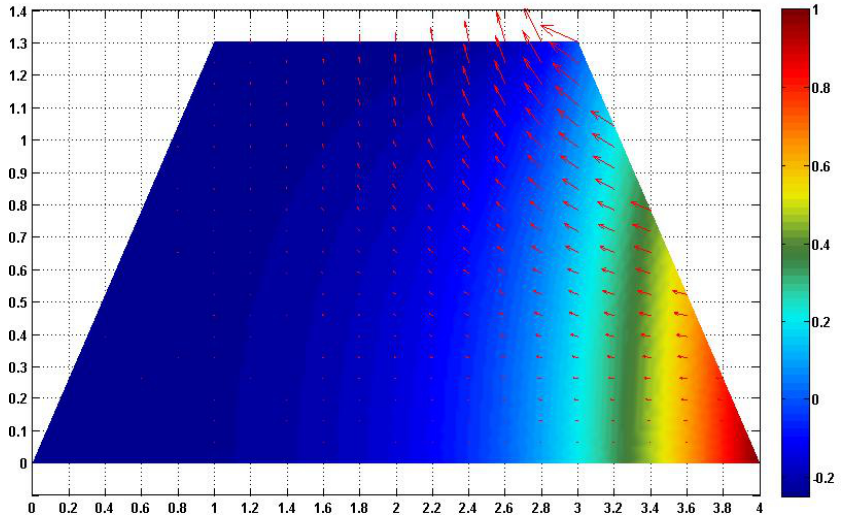

(e)

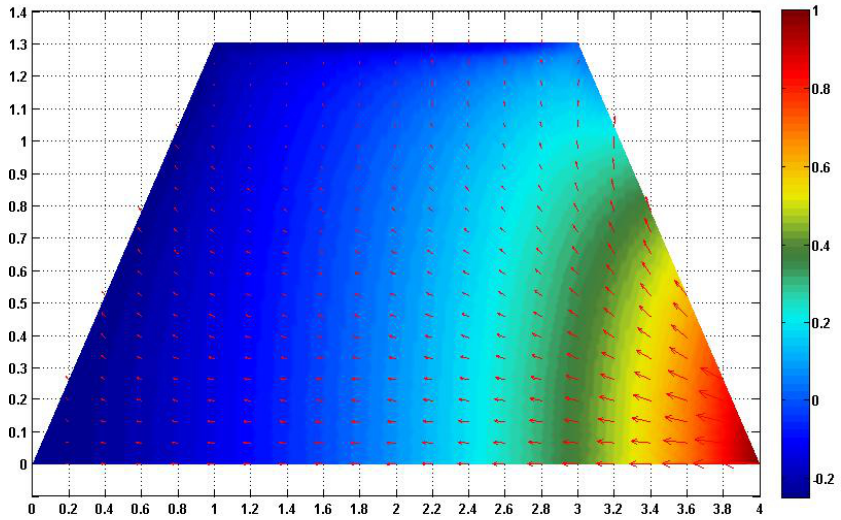

(f)

Figure 3.16: Pressure distributions for various permeabilities in a trapezoidal pile using a FEM. The permeabilities are given as (e) $\tilde{K} = \frac{10}{13}\tilde{y}$ and (f) $\tilde{K} = 1 - \frac{10}{13}\tilde{y}$.

ability while the rest of the domain has near-constant permeability defined by

$$\tilde{K}\left(\tilde{x},\tilde{y}\right)=1-0.9e^{-100(\tilde{y}-0.65)^2}. \tag{3.25}$$

Case (h) presents a low near-constant permeability with a narrow horizontal region of high permeability defined by

$$\tilde{K}\left(\tilde{x},\tilde{y}\right)=0.1+0.9e^{-100(\tilde{y}-0.65)^2}. \tag{3.26}$$

Case (g) shows fluid entering from the high pressure boundary in the bottom right corner and moving up and to the left until it reaches a region of no or small vertical flow along the blockage. The low permeability region has reduced the pressure near the boundary around $\tilde{y}=0.65$. Above the blockage, the fluid enters from the right face and exits through the low pressure boundary along the top face. In case (h), although there is some some fluid penetration into the pile, the bulk of the flow travels along the high permeability strip from the right face to the left face. This is similar to the cylindrical cases with the high permeability annulus, except the fluid is actually able to travel along the path defined by the hole from a high pressure region to a low pressure region.

Several observations were made in the FEM pile simulations that were also made in the porous cylinder simulations. In general, relative velocity will be higher in regions of high permeability than in regions of low permeability, as predicted by Darcy's law. Fluid will travel through the domain from a high pressure boundary to a low pressure boundary. Fluid will also take the path of least resistance flow along regions of high permeability as opposed to low permeability. Finally, the appropriate placement of a narrow low permeability layer appears to be able to prevent flow completely.

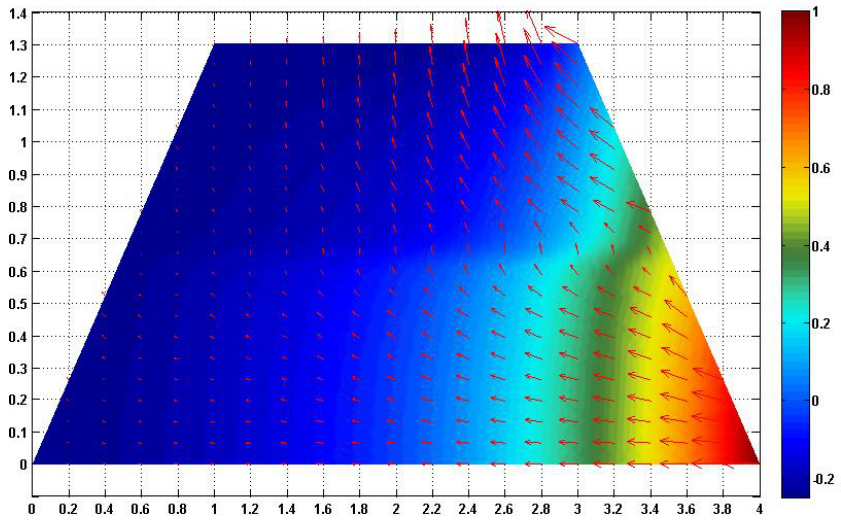

(g)

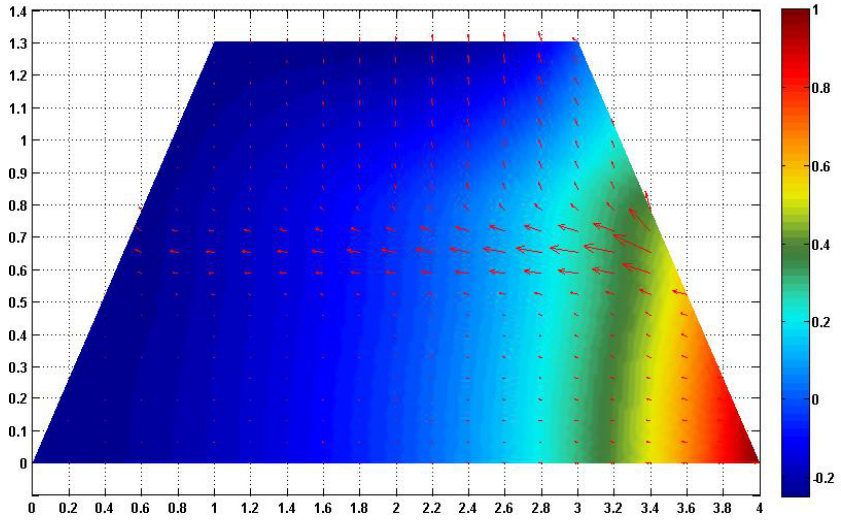

(h)

Figure 3.17: Pressure distributions for various permeabilities in a trapezoidal pile using a FEM. The permeabilities are given as (g) $\tilde{K} = 1 - 0.9e^{-100(\tilde{y}-0.65)^2}$, and (h) $\tilde{K} = 0.1 + 0.9e^{-100(\tilde{y}-0.65)^2}$.

Chapter 4

Unsteady Results

In the case of incompressible fluid flow with steady boundary conditions described in the previous chapter, the flow has zero dependence on time. In this chapter, a time-dependent model for slightly compressible fluid flow through a porous medium is developed, following reference [26]. An analytical solution for the constant permeability case and its tendency towards steady-state are examined. This model is built from the mass conservation equations for fluid and solid material in a porous medium, and assumes a functional relationship between fluid density and pressure in order to obtain a time-dependent equation. This differs somewhat from other studies, such as [9], which uses a two-layer model of incompressible fluid on top of a porous medium. In the fluid layer in that paper, time dependence is obtained through use of the Navier-Stokes equation and the heat conservation equation, while in the porous layer, the only time dependence occurs in the conservation of heat equation. This is coupled to Darcy's law with a buoyancy term by assuming fluid density to be temperature dependent.

4.1 A Time-Dependent Equation for Porous Media Flow

In this section, a time-dependent relationship for flow through a porous medium is derived through the method used by Verruijt [26] for the more general theory of consolidation. Instead of simply applying Darcy's law, the derivation begins with the mass balance equations for the fluid

$$\frac{\partial (\phi \rho_f)}{\partial t} + \nabla \cdot (\phi \rho_f \boldsymbol{u}) = 0, \tag{4.1}$$

and the solid medium,

$$\frac{\partial\left(\left(1-\phi\right)\rho_s\right)}{\partial t}+\nabla\cdot\left(\left(1-\phi\right)\rho_s\boldsymbol{w}\right)=0, \tag{4.2}$$

where ρ_f and ρ_s are the fluid and solid densities, respectively, $\boldsymbol{u}$ and $\boldsymbol{w}$ are the fluid and solid velocities, respectively, t is time, and ϕ is the porosity. It will be assumed later that the solid matter is rigid. Assuming the density of the porous material to be constant, this yields

$$-\frac{\partial\phi}{\partial t}+\nabla\cdot\left(\left(1-\phi\right)\boldsymbol{w}\right)=0. \tag{4.3}$$

When the Mach number (the ratio between the rate of flow and the speed of sound) is less than 0.3, as in the current case, flow is generally assumed to be incompressible. However, for the sake of deriving a time-dependent equation for flow through a porous medium, a functional relationship between the fluid density and pressure, p is assumed,

$$\rho_f=\rho_0 e^{\beta(p-p_0)}, \tag{4.4}$$

where β is the compressibility of the fluid, with units of length times time squared per mass, and ρ_0 and p_0 are reference values. Since $\beta\left(p-p_0\right)$ is generally very small, $e^{\beta(p-p_0)}$ is expected to be very close to 1, and thus the fluid density should only deviate slightly from the reference density. As such the fluid flow is expected to be only slightly compressible. This functional relationship gives the differential relationship

$$d\rho_f=\beta\rho_f dp. \tag{4.5}$$

From a thermodynamics point of view, this form of pressure dependence is somewhat unusual (for example, the ideal gas law gives a linear relationship between pressure and density), but as shown below, it gives a relatively simple method of incorporating compressibility effects in a pressure driven flow. Expanding equation (4.1), then applying this relationship and dividing by ρ_f yields

$$\frac{\partial\phi}{\partial t}+\phi\beta\frac{\partial p}{\partial t}+\nabla\cdot\left(\phi\boldsymbol{u}\right)+\beta\left(\nabla p\right)\cdot\left(\phi\boldsymbol{u}\right)=0. \tag{4.6}$$

By ignoring the second order nonlinear term $\beta\left(\nabla p\right)\cdot\left(\phi\boldsymbol{u}\right)$ (since the flow is expected to be rather weak), this equation is reduced to

$$\frac{\partial\phi}{\partial t}+\phi\beta\frac{\partial p}{\partial t}+\nabla\cdot\left(\phi\boldsymbol{u}\right)=0. \tag{4.7}$$

Adding equations (4.3) and (4.7) results in

$$\phi\beta\frac{\partial p}{\partial t} + \nabla \cdot [\phi\,(\boldsymbol{u} - \boldsymbol{w})] + \nabla \cdot \boldsymbol{w} = 0. \tag{4.8}$$

Assuming the porous medium is stationary implies $\boldsymbol{w} = \boldsymbol{0}$. Therefore, for slightly compressible fluid flow through a stationary porous medium with constant porosity, pressure is related to the fluid velocity, $\boldsymbol{u}$, through the equation

$$0 = \beta\frac{\partial p}{\partial t} + \nabla \cdot \boldsymbol{u}. \tag{4.9}$$

Taking the divergence of Darcy's law and substituting it into (4.9) yields an equation with pressure as the only unknown,

$$\beta\frac{\partial p}{\partial t} = \nabla \cdot \left(\frac{K}{\mu}\nabla p\right). \tag{4.10}$$

Rearranging equation (4.10) gives,

$$\frac{\partial p}{\partial t} = \frac{1}{\beta\mu}\nabla \cdot (K\nabla p). \tag{4.11}$$

Using the dimensionless variables described in the previous chapter, and introducing the dimensionless time variable $\tilde{t} = \omega t$, where ω is the characteristic frequency scale, (4.10) can be nondimensionalized to give

$$\frac{\partial P}{\partial \tilde{t}} = D\tilde{\nabla} \cdot \left(\tilde{K}\tilde{\nabla}P\right), \tag{4.12}$$

where

$$D = \frac{K_{\text{Ref}}}{R^2\omega\beta\mu}. \tag{4.13}$$

4.2 Constant Permeability Solution

For the constant permeability case, the time-dependent equation becomes

$$\frac{\partial P}{\partial \tilde{t}} = D\tilde{\nabla}^2 P, \tag{4.14}$$

where the dimensional permeability $K = K_{\text{Ref}}$ and D is defined as above. The solution to this equation can be expressed as the sum of a steady-state solution, $P_{SS}(\tilde{r}, \theta)$, as

determined in the previous chapter, and the time-dependent particular solution, $\bar{P}\left((\tilde{r},\theta,\tilde{t}\right)$. Expanding the right-hand side of the time-dependent pressure equation in polar coordinates yields

$$\frac{\partial P}{\partial \tilde{t}} = D\left(\frac{\partial^2 P}{\partial \tilde{r}^2} + \frac{1}{\tilde{r}}\frac{\partial P}{\partial \tilde{r}} + \frac{1}{\tilde{r}^2}\frac{\partial^2 P}{\partial \theta^2}\right). \tag{4.15}$$

Since the steady-state solution is independent of time and solves the equation

$$\tilde{\nabla}^2 P_{SS} = 0 \tag{4.16}$$

exactly, only the particular solution to the equation

$$\frac{\partial \bar{P}}{\partial \tilde{t}} = D\tilde{\nabla}^2 \bar{P} = D\left(\frac{\partial^2 \bar{P}}{\partial \tilde{r}^2} + \frac{1}{\tilde{r}}\frac{\partial \bar{P}}{\partial \tilde{r}} + \frac{1}{\tilde{r}^2}\frac{\partial^2 \bar{P}}{\partial \theta^2}\right) \tag{4.17}$$

is sought. The particular solution can be expressed as the difference between the complete solution and the steady-state solution,

$$\bar{P}\left(\tilde{r},\theta,\tilde{t}\right) = P\left(\tilde{r},\theta,\tilde{t}\right) - P_{SS}(\tilde{r},\theta). \tag{4.18}$$

The boundary conditions for the particular solution are therefore

$$\bar{P}\left(1,\theta,\tilde{t}\right) = P\left(1,\theta,\tilde{t}\right) - P_{SS}(1,\theta). \tag{4.19}$$

As in the previous section, the boundary conditions for the steady-state problem describing a turbulent flow about a cylinder are taken to be an even function defined by a cosine series

$$P_{SS}(1,\theta) = \sum_{n=0}^{N} a_n \cos\left(n\theta\right). \tag{4.20}$$

In the long-time limit of the time-dependent problem, the steady-state solution is therefore

$$P_{SS}(\tilde{r},\theta) = \sum_{n=0}^{N} a_n \tilde{r}^n \cos\left(n\theta\right). \tag{4.21}$$

For the time-dependent problem, it is assumed that the initial pressure distribution at $\tilde{t} = 0$ is 0 everywhere in the cylinder. The steady-state boundary conditions are used as forcing, and are assumed to switch on instantaneously at $\tilde{t} = 0$. Mathematically, this is given as

$$P\left(1,\theta,\tilde{t}\right) = H\left(\tilde{t}\right) P_{SS}(1,\theta), \tag{4.22}$$

where $H\left(\tilde{t}\right)$ is the Heaviside function, which is slightly modified from its usual description, such that

$$H\left(\tilde{t}\right) = \begin{cases} 0 & \tilde{t} \leq 0, \\ 1 & \tilde{t} > 0. \end{cases}$$

Using these initial and boundary conditions for the full time-dependent problem, for $\bar{P}$, the initial conditions are

$$\bar{P}(\tilde{r}, \theta, 0) = -P_{SS}(\tilde{r}, \theta), \tag{4.23}$$

while the boundary conditions are

$$\bar{P}\left(1, \theta, \tilde{t}\right) = 0 \tag{4.24}$$

for $\tilde{t} > 0$. Both Özışık [21] and Haberman [11] apply the separation of variables technique to solve this diffusion problem. In this case, it is assumed that the particular solution is separable in terms of $\tilde{r}$, θ, and $\tilde{t}$, i.e., $\bar{P}\left(\tilde{r}, \theta, \tilde{t}\right) = f(\tilde{r})g(\theta)h\left(\tilde{t}\right)$. Entering this into equation (4.17) and dividing by $\bar{P}$ results in

$$\frac{1}{D}\frac{h'}{h} = \frac{f''}{f} + \frac{1}{\tilde{r}}\frac{f'}{f} + \frac{1}{\tilde{r}^2}\frac{g''}{g}. \tag{4.25}$$

Since f,g, and h are all functions of a different variable, in order to solve (4.25), it must be true that

$$\frac{1}{D}\frac{h'}{h} = -\alpha^2, \tag{4.26}$$

and

$$\frac{g''}{g} = -\zeta^2, \tag{4.27}$$

where α and ζ are separation constants, and the minus sign and the power of two have been chosen for convenience. These constants also yield a differential equation for f,

$$0 = f'' + \frac{1}{\tilde{r}}f' + \left(\alpha^2 - \frac{\zeta^2}{\tilde{r}^2}\right) f. \tag{4.28}$$

Solving the first two differential equations yields

$$h\left(\tilde{t}\right) = c_1 e^{-\alpha^2 D\tilde{t}}, \tag{4.29}$$

and

$$g(\theta) = c_2 \cos(\zeta\theta) + c_3 \sin(\zeta\theta), \tag{4.30}$$

where c_1, c_2, and c_3 are constants dependent on the initial and boundary conditions. Since the flow past the cylinder is identical to the flow described in the previous chapter, the boundary conditions will be even across the x-axis. This implies that g is dependent on the even function cosine only,

$$g(\theta) = c_2 \cos(\zeta\theta). \tag{4.31}$$

Applying periodicity to this problem implies $\bar{P}\left(\tilde{r}, 0, \tilde{t}\right) = \bar{P}\left(\tilde{r}, 2\pi, \tilde{t}\right)$, or $g(0) = g(2\pi)$. This suggests that $\zeta = n$, where $n = 0, 1, 2, \ldots$.

The differential equation in terms of f is the well-known Bessel's equation, the solution of which is expressed as the sum of the Bessel function of the first kind,

$$J_\zeta(\alpha\tilde{r}) = \sum_{k=0}^{\infty} \frac{(-1)^k \left(\alpha\tilde{r}/2\right)^{2k+\zeta}}{k!\,(k+\zeta)!} \tag{4.32}$$

and the Bessel function of the second kind, using the commonly used z for its argument and m for the order of the function,

$$Y_m(z) = \frac{2}{\pi}\left[\left(\log\frac{z}{2} + \gamma\right) J_m(z) - \frac{1}{2}\sum_{k=0}^{m-1} \frac{(m-k-1)!\left(z/2\right)^{2k-m}}{k!}\right. \tag{4.33}$$

$$\left. + \frac{1}{2}\sum_{k=0}^{\infty}(-1)^{k+1}[\varphi(k) + \varphi(k+m)]\frac{\left(z/2\right)^{2k+m}}{k!(k+m)!}\right], \tag{4.34}$$

that is,

$$f(\tilde{r}) = c_4 J_\zeta(\alpha\tilde{r}) + c_5 Y_\zeta(\alpha\tilde{r}), \tag{4.35}$$

where c_4 and c_5 are constants to be determined based on the boundary conditions. Note that in the Bessel function of the second kind,

$$\varphi(k) = \sum_{j=1}^{k} \frac{1}{j}, \tag{4.36}$$

$\varphi(0) = 0$, and γ is Euler's constant [11]. Since $Y_\zeta(\alpha r)$ tends to negative infinity as r tends to zero, the Bessel function of the second kind should be dropped in order to give a physically realistic solution. Using this and the fact that $\zeta = n$,

$$f(\tilde{r}) = c_4 J_n(\alpha\tilde{r}). \tag{4.37}$$

Based on the boundary conditions for $\bar{P}\left(1, \theta, \tilde{t}\right) = f(1)g(\theta)h\left(\tilde{t}\right) = 0$, in order to obtain a non-trivial solution, $f\,(1)$ must be 0. From this the eigenvalue α can be discerned. Since

$$0 = J_n(\alpha), \tag{4.38}$$

it can be inferred that the values of α are the zeros of the Bessel function, z_{nm}, such that m is the mth root of $J_n(z)$. This results in the general form of the particular solution being

$$\bar{P}\left(\tilde{r},\theta,\tilde{t}\right) = -\sum_{m=1}^{\infty}\sum_{n=0}^{N} c_{nm}J_n(z_{nm}\tilde{r})\cos(n\theta)e^{-z_{nm}^2 D\tilde{t}}, \tag{4.39}$$

where c_{nm} is some constant that can be determined based on the initial conditions. Unfortunately, due to the nature of the Bessel function, determining the constant through comparison with the steady-state solution is rather difficult, and is unnecessary for the remainder of the discussion. It is important to note that for each n, the Bessel function has an infinite number of increasing roots such that $z_{n0} < z_{n1} < \ldots < z_{nm} < z_{nm+1} < \ldots$. Similarly, for fixed m, as n increases, so does z_{nm}, e.g., the first root of J_1 is greater than the first root of J_0, the sixth root of J_4 is greater than the sixth root of J_3, etc. These facts are demonstrated in Figure 4.1, which plots the the first several roots of the first three Bessel functions of the first kind. Since $z_{nm}^2 D$ determines the rate of decay in the particular solution, this fact implies that the higher mode components to the solution will tend to the steady-state solution faster than the lower mode components. This is demonstrated in Figure 4.2. The $n = 1$ and the $n = 5$ modes of the solution of equation (4.12) are numerically computed in Fourier space using the method described in Chapter 3 for the spatial component (without transforming back into the angular coordinate), and the fully implicit backwards Euler scheme for the time component. Note that 82 Chebyshev grid points have been used in the radial direction in this case. In this simulation, $\Delta\tilde{t} = 0.1$ and D has been set to 10^{-3}. This choice of D is not based on any physical parameters, but has been selected to illustrate the behaviour of each of the components of the solution. Additionally, constant boundary conditions are used for the sake of this discussion, as opposed to the conditions dependent on θ used in deriving the above solution. In Figure 4.2, the $n = 5$ mode appears to remain constant and reach the steady-state very quickly, while the $n = 1$ mode is still decaying. This may be better illustrated in Figure 4.3, which plots the difference between the time-dependent solution in Fourier space and the the steady-state solution in Fourier space for the $n = 1$ and $n = 5$ modes over time. Within 200 dimensionless time units, the difference between the $n = 5$ components has decreased to $\mathcal{O}\left(10^{-6}\right)$, while the difference in the $n = 1$ components is $\mathcal{O}\left(1\right)$.

Bessel's equation can also be expressed in the form of a Sturm-Liouville problem by multiplying equation (4.28) by $\tilde{r}$,

$$0 = \frac{\partial}{\partial\tilde{r}}\left(\tilde{r}\frac{\partial f}{\partial\tilde{r}}\right) - \frac{\zeta^2}{\tilde{r}}f + \alpha^2\tilde{r}f. \tag{4.40}$$

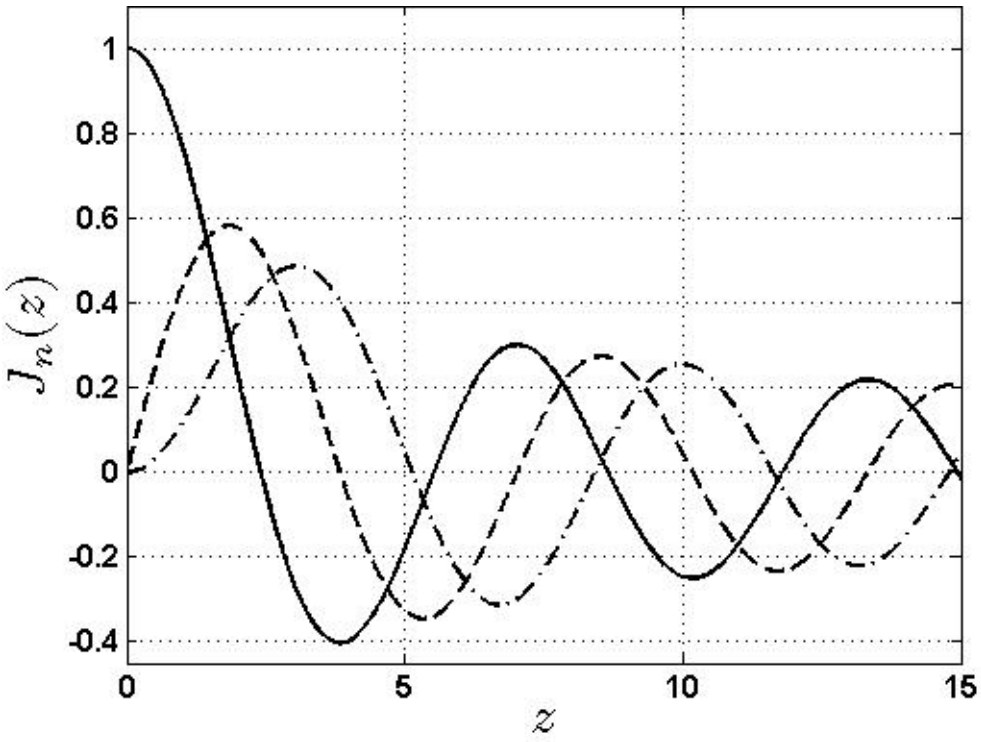

Figure 4.1: The first three Bessel functions, $J_0(z)$ (solid line), $J_1(z)$ (dashed line), $J_2(z)$ (dot-dashed line).

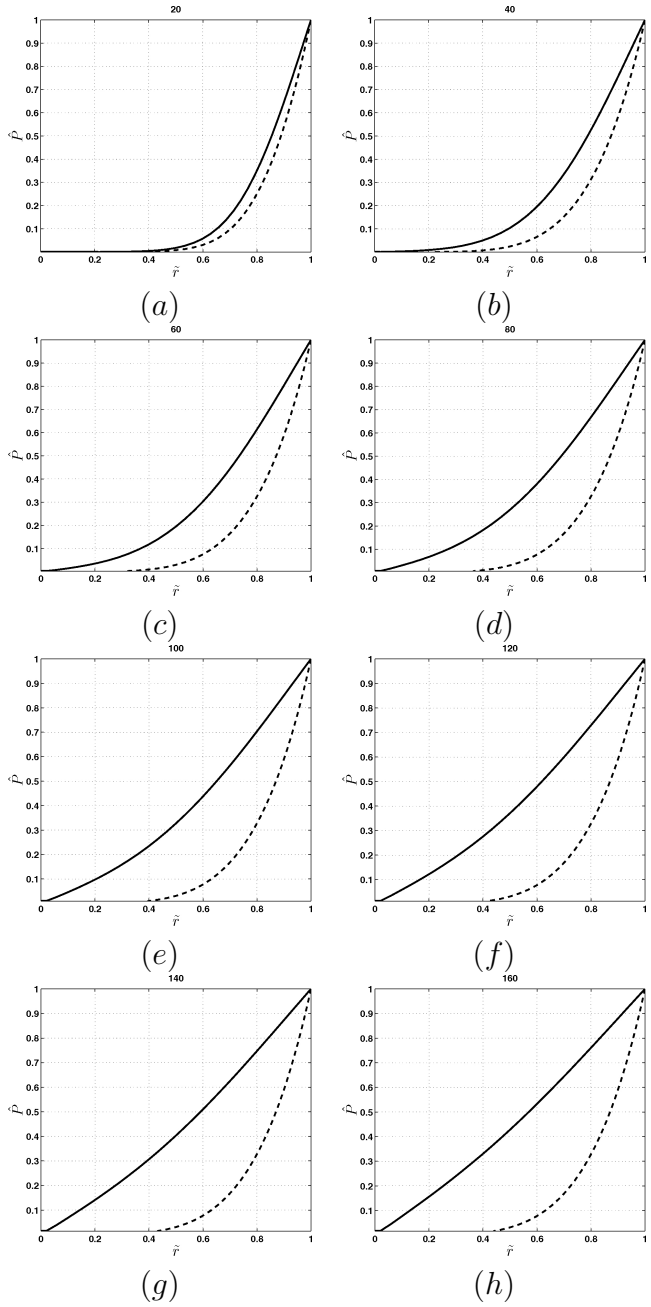

Figure 4.2: The $n = 1$ mode (solid line) and $n = 5$ mode (dashed line) for the time-dependent solution for pressure in Fourier space as they tend to steady-state over time. The dimensionless time values for the plots are found above each graph.

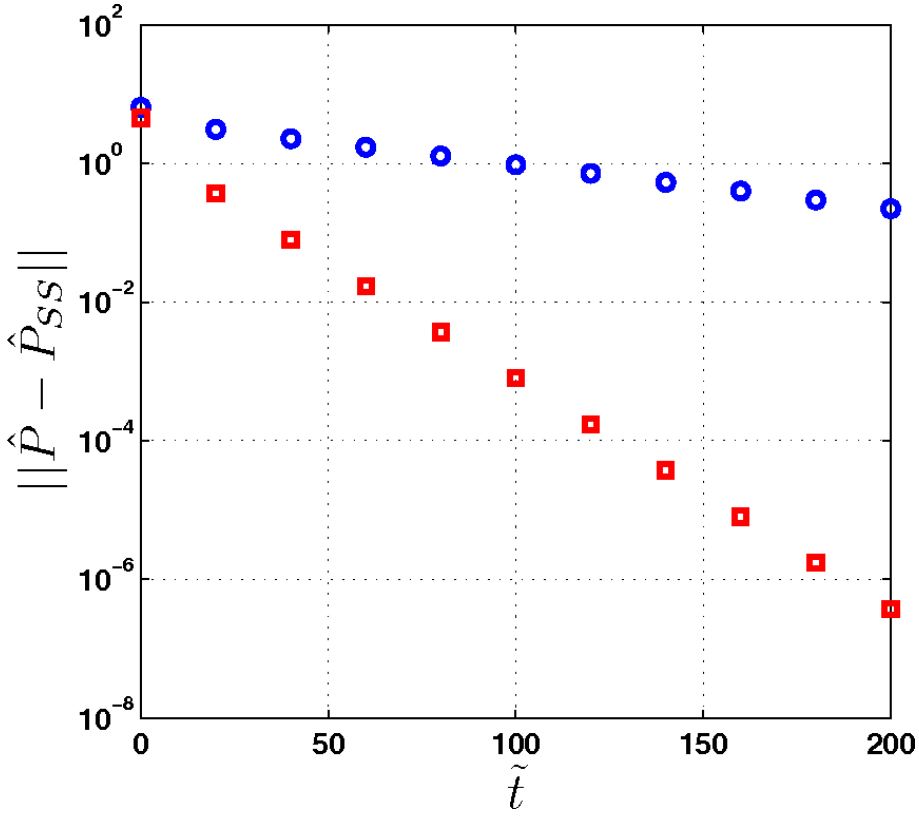

Figure 4.3: Logarithmic plot between the difference in the time-dependent solution and the steady-state solution in Fourier space over time. The circles indicate the $n = 1$ mode component, while the squares indicate the $n = 5$ mode component. The higher mode component is shown to tend to the steady-state solution faster than the lower mode component.

When compared to the Sturm-Liouville problem described in the Methodology section, $p = \tilde{r}$, $q = -\frac{\zeta^2}{\tilde{r}}$, $\sigma = \tilde{r}$ and $\lambda = \alpha^2$. This is not, however, a regular Sturm-Liouville problem since $\tilde{r} = 0$ is within the domain of the cylinder, and thus p and σ are non-positive on the domain, and q is discontinuous as it tends to $-\infty$ as $\tilde{r}$ tends to 0. Additionally, the boundary condition is not defined in the appropriate way for a Sturm-Liouville problem at $\tilde{r}$. This is, in fact, a singular Sturm-Liouville problem. In spite of this, some theorems for regular Sturm-Liouville problems still hold for this equation, such as the theorem stating that there exists an infinite number of eigenvalues [11]. Also, for fixed n, orthogonality with respect to the weight function $\tilde{r}$ between the $J_n(z_{nm}\tilde{r})$ for different values of m is maintained [11].

Figures 4.4 and 4.5 display the time evolution of air flow through a constant permeability porous disc with zero initial conditions on the interior, and turbulent forcing boundary conditions as described earlier in the chapter ($P(\tilde{r}, \theta, 0) = 0$ and $P\left(1, \theta, \tilde{t}\right) = H\left(\tilde{t}\right) P_{SS}(1, \theta)$). As described for the time evolution of the individual modes, the time-dependent code treats the spatial component in the same way as the steady-state code, with a Chebyshev spectral method in the radial direction, and a Fourier spectral method in the azimuthal direction. The time component is computed using a fully implicit backwards Euler scheme. The resulting system is solved with Matlab's direct solver (backslash). For the current simulation, the physical parameters were set to $R = 15\,\mathrm{m}$, the height of the test piles at the Diavik site, $K_{\mathrm{Ref}} = 10^{-12}\,\mathrm{m}^2$, the lower bound of permeability values computed for the Diavik test piles [10], and $\mu = 1.71 \times 10^{-5}\,\mathrm{kg/m\,s}$, the dynamic viscosity for dry air at 0°C [15]. For an ideal gas, isothermal compressibility β is equal to $1/p$ [7]. Whether it is consistent to keep β constant may be an issue when examining future work, as in the derivation of the time-dependent problem, β was assumed to be constant. For the sake of parameterization, a constant reference pressure will be chosen, specifically the standard atmospheric pressure of $1\,\mathrm{atm} = 101.325\,\mathrm{kPa} = 101325\,\mathrm{kg/m\,s^2}$, therefore, $\beta = 1\,\mathrm{m\,s^2}/101325\,\mathrm{kg}$. This assumption should be valid as the pressure inside the pile is not expected to experience particularly large deviations from the external pressure. A 162 point Chebyshev grid has been used in the radial direction, and 80 grid points have been used in the azimuthal direction. As a note, all values in these profiles are dimensionless.

Initially, on small dimensionless time scales, such as $\Delta\tilde{t} = 0.001$, which corresponds to 1.44 minutes in dimensional time, noticeable changes in the pressure profile are observed, although these changes become much less pronounced as time increases. The simulation begins by decreasing to the large negative pressure near the boundaries around $\theta = \pi/2$ and $\theta = 3\pi/2$ and increasing to the large positive pressure near the boundary around $\theta = 0$. The pressure then continues to decrease throughout most of the cylinder's interior except near the large positive pressure boundary until it reaches the steady-state. Between

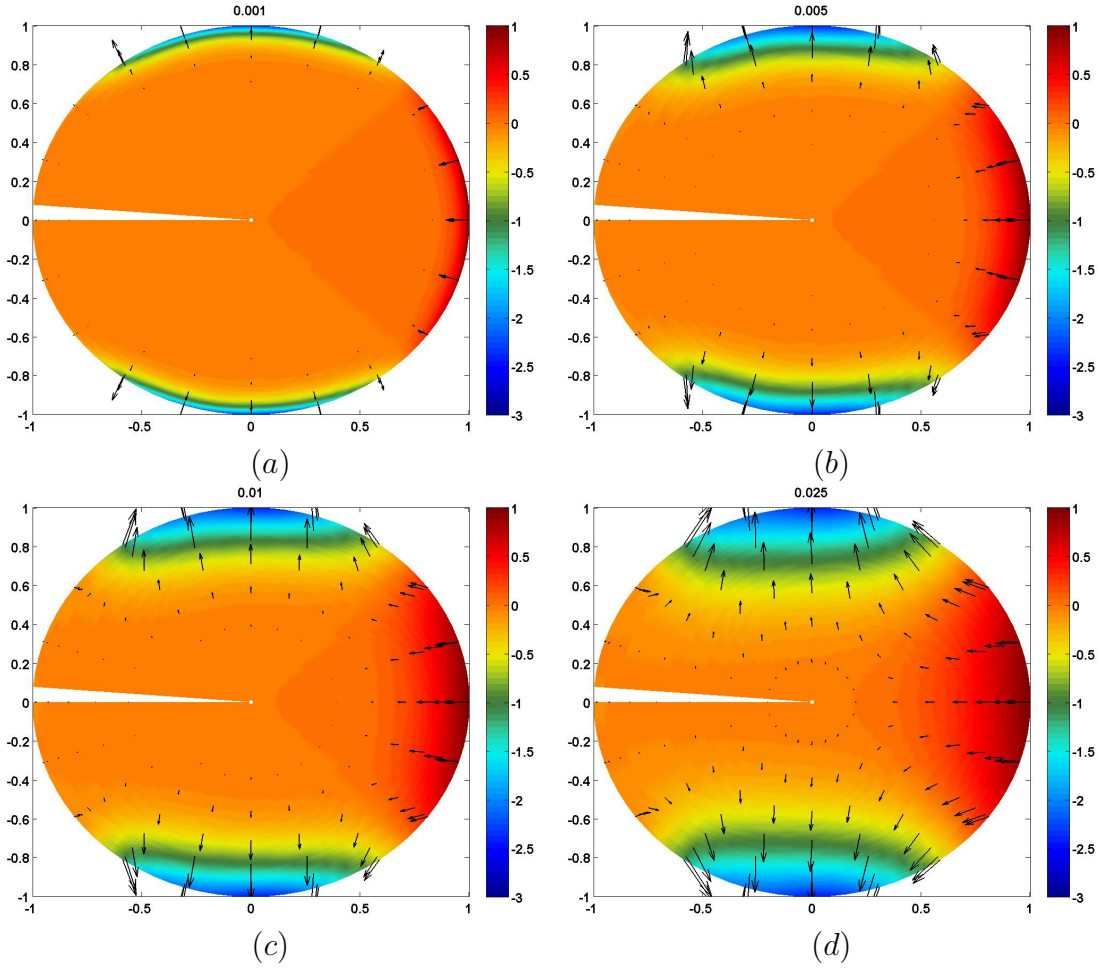

Figure 4.4: Pressure profiles and velocity fields for time-dependent flow through a constant permeability cylinder with $D = 2.28$. The dimensionless time values at which each profile was plotted are found above each graph. Additional profiles at later times are presented in Figure 4.5.

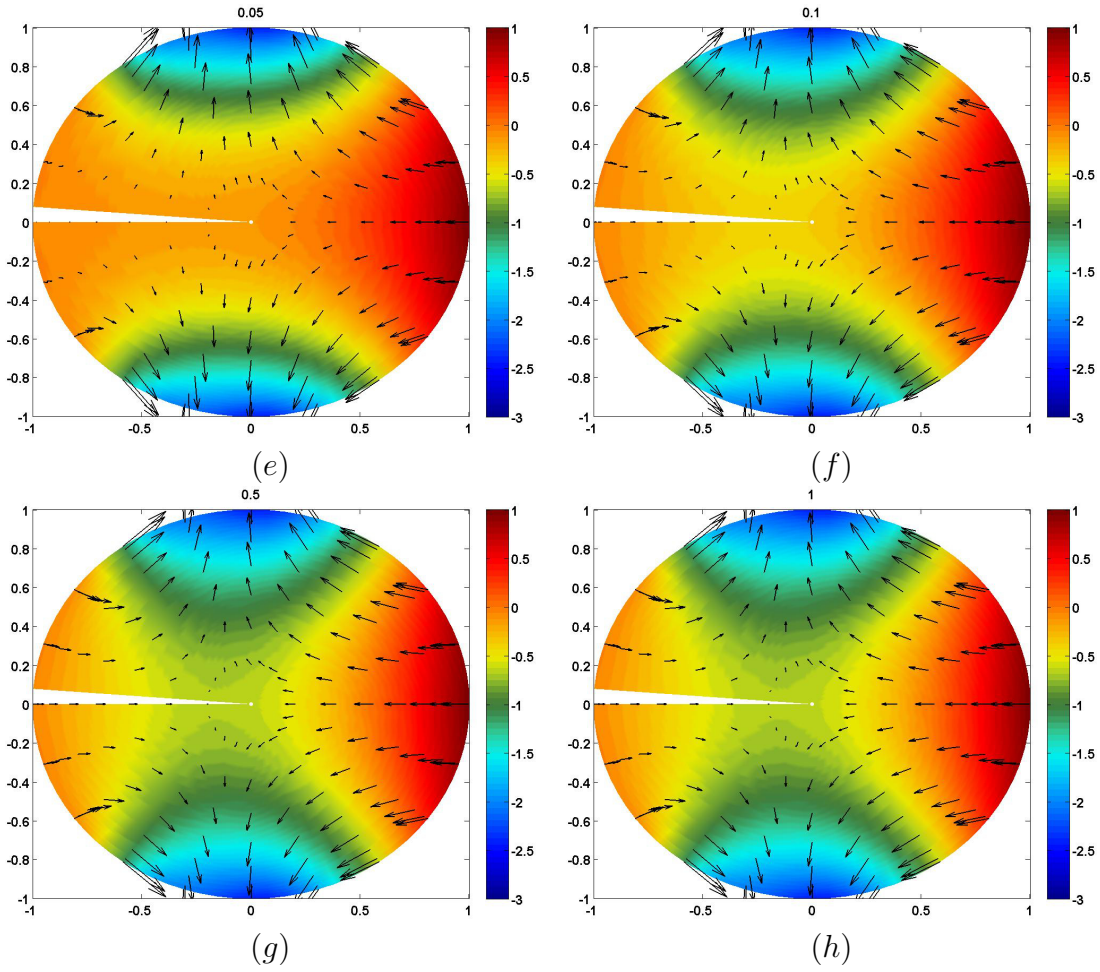

Figure 4.5: Additional pressure profiles and velocity fields for time-dependent flow through a constant permeability cylinder with $D = 2.28$. The dimensionless time values at which each profile was plotted are found above each graph.

$\tilde{t} = 0.1$ and $\tilde{t} = 0.5$, the changes on small time scales become difficult to perceive, and only changes on larger time scales are noticeable. It is within this range that the solution has decayed very close to the steady-state solution, though some small fluctuations may still be visible.

The sensitivity to time dependence of the unsteady model also requires further critical examination. Depending on the physical parameters of the situation being modeled, the particular solution of the constant permeability slightly compressible fluid problem may be completely negligible. It may be satisfactory to model the problem with the steady-state equation only through a parametric dependence on time dependent boundary conditions. Using the above parameters R, μ and β, the coefficient D in equation (4.12) may range from $2.6335 \times 10^{-5}/\omega$ to $2.6335/\omega$ for $K_{\text{Ref}} = 10^{-12}\text{m}^2$ to $K_{\text{Ref}} = 10^{-7}\text{m}^2$, that is, the range of permeabilities determined for the Diavik test piles [10]. The only remaining factor is to determine the length of the characteristic time scales. The larger the time scale, the greater the constant D, and the less time dependence is exhibited. According to [10] the dominant wind events occur on a scale of 1 to 50 days. This implies that for the lowest time scale of 1 day, $D = 2.28$, and as shown in the above simulation, after about half a day the changes in flow appear to be insignificant. For longer time scales, the time-dependent effects will only decay faster, so for time scales on the order of days, time dependence is expected to become negligible very quickly. This suggests that for the long term operational periods for the mine, steady-state modeling may be sufficient.

Chapter 5

Discussion and Conclusions

While some of the conclusions were mentioned as a part of the discussion of the results, they are repeated in this section for the reader's convenience. A pressure driven flow has been modeled through a porous pile using spectral and finite element methods, with an emphasis on the former. Because the field situation is expected to yield a high Reynolds number for flow outside the pile, care was taken to represent the turbulent aspect of the forcing. Since detailed data for the actual shape of the waste rock piles was not available, the well-studied case of a cylinder, for which well-validated turbulent pressure distributions can be found, was the focus of this research. In the separation region, pressure about a cylinder is nearly constant, and since Darcy's law is a linear equation, in this thesis the pressure in this region was set to near zero. As a result, the pressure gradient in the turbulent situation is much smaller than in the classical case of potential flow about the cylinder, and thus, there is less flow in the porous region. To discourage flow in waste rock piles, and therefore oxygen transport and AMD, it is thus prudent for construction to ensure that separation occurs as close as possible to the forward stagnation point. In general, once the critical Reynolds number for a cylinder, $\mathrm{Re}_{Cr} \sim 3 \times 10^5$ [15], is reached, as Reynolds number increases, the angle at which separation occurs increases. This would suggest that by controlling the Reynolds number of the flow, one should be able to control the region of separation. Unfortunately, controlling the Reynolds number would mean either changing the wind speed or kinematic viscosity, which is impossible since they are dictated by natural processes, or controlling the characteristic length scale of the pile, which may not be feasible, due to the amount of rock that may need to be stored. The solution is to therefore modify the pile geometry or build some sort of obstacle, such as a fence, so that as much separation occurs over the pile as possible. The pile geometry should also be aligned with the dominant wind speeds, and this may not be possible in all

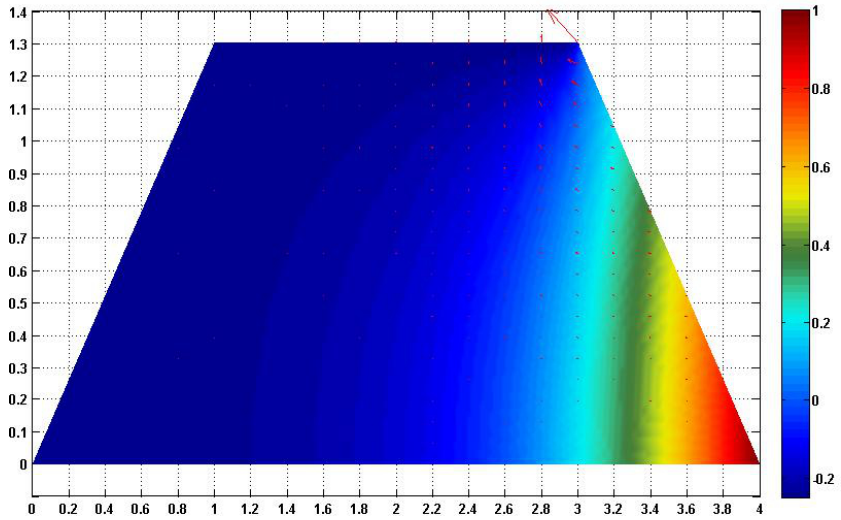

Figure 5.1: Pressure distribution and velocity field through a pile with permeability $\tilde{K}(\tilde{x}, \tilde{y}) = \frac{10}{13}\tilde{y}$ where turbulence is induced at the top right corner of the pile.

field situations.

Through the simulations in this thesis, several factors were shown to affect pressure distributions and flow profiles through porous domains. Narrow regions of low permeability were shown to be able to block flow almost completely. Fluid was observed to travel along narrow paths of high permeability surrounded by regions of low permeability if the pressure gradient between the entrance and exit points is large enough. Low permeability regions near high pressure boundaries seem to be able to reduce the amount of fluid penetration. For cases where the high pressure region is near the base of the pile, such as the trapezoidal case examined in the Steady Results chapter, this can be used in conjunction with early onset of turbulence to significantly reduce flow through the pile, as demonstrated in Figure 5.1. This simulation uses a permeability that increases as a function of $\tilde{y}$, $\tilde{K}(\tilde{x}, \tilde{y}) = \frac{10}{13}\tilde{y}$, so permeability is small near the high pressure boundary. Along the top face, it is assumed that turbulence begins at the upper right corner, perhaps through fence or snow wall construction, and pressure has been set to the small constant -0.25. The remaining boundary conditions are those described in Chapter 3. This results in practically zero flow through the domain except in the upper right corner. It should be relatively simple and inexpensive to implement the suggested setup in practice by ensuring that the final few loads of waste rock dumped down the upwind face is made up of finely crushed material. Of course, the approach will require experimental and field validation to

assess its practical effectiveness.

For time scales on the order of days, it was shown that slightly compressible flow quickly tends to the steady-state as time dependence becomes negligible. In general, higher mode components of the time-dependent solution were shown to decay faster than lower mode components.

The model presented in this thesis is far from complete when accounting for all factors that drive flow through waste rock piles. As mentioned in the Introduction, heat flow and chemical reaction effects also play important roles in waste rock pile flow, and should thus be included. For fluid flow through a porous medium, conservation of energy can be defined by the equation

$$\rho_f c_{f_p} \left(\frac{\partial T}{\partial t} + \boldsymbol{u} \cdot \nabla T \right) = k_f \nabla^2 T + Q, \tag{5.1}$$

where ρ_f is the fluid density, c_{f_p} is the specific heat constant of the fluid at constant pressure, and k_f is the thermal conductivity of the fluid [4]. Q is a function representing the heat source, most importantly the exothermic sulfide oxidation reaction. The concentration of oxygen in the air flowing through the pile, C, satisfies the mass balance equation

$$\frac{\partial C}{\partial t} + \boldsymbol{u} \cdot \nabla C = D \nabla^2 C + R(C), \tag{5.2}$$

where D is the mass diffusivity, and $R(C)$ is a function that describes the consumption of oxygen by the pyrite oxidation reaction. Although it will complicate matters, it may be wise for Q and R to have some oxygen concentration and temperature dependence, respectively, since the amount of heat produced will depend on the amount of oxygen being consumed, and it is well-known that reaction rate depends on temperature. For the sake of accounting for all physical effects, rewriting Darcy's law with buoyancy yields,

$$\frac{\mu}{K} \boldsymbol{u} = -\nabla p - \rho_f g \hat{k}, \tag{5.3}$$

where g is the gravitational acceleration constant and $\hat{k}$ is the unit vector in the z-direction. In the steady-state limit, Darcy's law remains unchanged, while the heat and concentration conservation equations become

$$\rho_f c_{f_p} \boldsymbol{u} \cdot \nabla T = k_f \nabla^2 T + Q \tag{5.4}$$

and

$$\boldsymbol{u} \cdot \nabla C = D \nabla^2 C + R(C), \tag{5.5}$$

respectively. Although this does remove the time dependence, the presence of the $\boldsymbol{u}\cdot\nabla$ term in each equation still causes nonlinearity, resulting in further modeling difficulties. Further examination of this complete model is a logical next step for this research. Implementing time-dependent forcing may also be beneficial, as it can be used to simulate various wind and weather effects. This may lead to a more realistic model, as weather conditions are very rarely static.

References

[1] R. D. Anne and G. Pantelis. Coupled natural convection and atmospheric wind forced advection in above ground reacting heaps. *International Conference on Computational Fluid Dynamics in Mineral and Metal Processing and Power Generation*, pages 453 – 458, July 1997.

[2] O. Axelsson and V. A. Barker. *Finite Element Solution of Boundary Value Problems: Theory and Computation*. Classics in Applied Mathematics. Society for Industrial and Applied Mathematics, 1984.

[3] J. B. Bates. Fourier transform infrared spectroscopy. *Science*, 191(4222):31 – 37, January 1976.

[4] A. Bejan. *Convection heat transfer*. John Wiley & Sons, Incorporated, 2004.

[5] J. W. Bennett, A. M. Garvie, G. Pantelis, A. I. M. Ritchie, A. V. Bell, and M. Noel. Comparison of measured and predicted transport processes controlling oxidation in the waste rock piles at the Heath Steele mine site. *Sudbury '95, Conference on mining and the environment*, pages 1017 – 1026, May/June 1995.

[6] M. Berggren. *An Introduction to the Finite Element Method for Elliptic Problems*. Uppsala University Department of Scientific Computing, 2002.

[7] R.S. Berry, S.A. Rice, and J. Ross. *Physical Chemistry*. Topics in Physical Chemistry. Oxford University Press, 2000.

[8] W. E. Boyce and R. C. DiPrima. *Elementary Differential Equations and Boundary Value Problems*. John Wiley & Sons, Incorporated, 2004.

[9] M. Carr. Penetrative convection in a superposed porous-medium-fluid layer via internal heating. *J. Fluid Mech.*, 509:305 – 329, 2004.

[10] X. Chi. Characterizing low-sulfide instrumented waste-rock piles: image grain-size analysis and wind-induced gas transport. Master's thesis, University of Waterloo, 2010.

[11] R. Haberman. *Applied Partial Differential Equations: With Fourier Series and Boundary Value Problems*. Pearson Prentice Hall, 2004.

[12] J.R. Harries and A. I. M. Ritchie. The impact of rehabilitation measures on the physicochemical conditions within mine wastes undergoing pyritic oxidation. *Proc. of the Sixth Int. Symp. on Biohydrometallurgy*, pages 341 – 351, August 1986.

[13] Diavik Diamond Mines Inc. *Diavik Diamond Mine Fact Book*. 2009.

[14] R. Klock, E. Hudson, D. Aihoshi, and J. Mullock. *The Weather of the Yukon, Northwest Territories and Western Nunavut: Graphic Area Forecast 35*. NAV CANADA, 2001.

[15] P. K. Kundu and I. M. Cohen. *Fluid Mechanics*. Academic Press, 2008.

[16] R. Lefebvre, D. Hockley, J. Smolensky, and P. Glinas. Multiphase transfer processes in waste rock piles producing acid mine drainage: 1: Conceptual model and system characterization. *Journal of Contaminant Hydrology*, 52:137 – 164, 2001.

[17] R. Lefebvre, D. Hockley, J. Smolensky, and A. Lamontagne. Multiphase transfer processes in waste rock piles producing acid mine drainage: 2. Applications of numerical simulation. *Journal of Contaminant Hydrology*, 52:165 – 186, 2001.

[18] V. K. Madisetti. *The Digital Signal Processing Handbook: Digital signal processing fundamentals*. The Electrical Engineering Handbook Series. CRS Press / Taylor & Francis Group, 2010.

[19] MathWorks. *Partial Differential Equation Toolbox User's Guide*. MathWorks, Incorporated, 2012.

[20] D. A. Nield and A. Bejan. *Convection in porous media*. Springer, 2006.

[21] M. N. Özışık. *Boundary value problems of heat conduction*. Dover classics of science and mathematics. Dover Publications, 1989.

[22] M. Schoonen, A. Elsetinow, M. Borda, and D. Strongin. Effect of temperature and illumination on pyrite oxidation between ph 2 and 6. *Geochem. Trans.*, 1:23 – 33, 2000.

[23] D. Siegel. *Applied Math 753 Advanced Partial Differential Equations Course Notes*. University of Waterloo, 2010.

[24] M. Stastna. *Applied Math 361 Continuum Mechanics Course Notes*. University of Waterloo, 2012.

[25] L. N. Trefethen. *Spectral Methods in Matlab*. Software, Environments, Tools. Society for Industrial and Applied Mathematics, 2000.

[26] A. Verruijt. *Computational geomechanics*. Theory and applications of transport in porous media. Kluwer Academic, 1995.